LASER
& PHOTONICS
REVIEWS

Supporting Information

for *Laser Photonics Rev.*, DOI 10.1002/lpor.202300980

All-Dielectric High-Q Dynamically Tunable Transmissive Metasurfaces

*Ruzan Sokhoyan, Claudio U. Hail, Morgan Foley, Meir Y. Grajower and Harry A. Atwater**

Supporting Information

All-dielectric high-Q dynamically tunable transmissive metasurfaces

*Ruzan Sokhoyan, Claudio U. Hail, Morgan Foley, Meir Y. Grajower, and Harry A. Atwater**

1. Extraction of the quality factor and Fano phase

We extracted the quality factor and Fano phase values by fitting the transmittance spectra to the Fano formula:[1]

$$T = A\frac{\left|\frac{\gamma_0}{2} - e^{-2i\Delta}\left(i(\omega-\omega_0) - \frac{\gamma_0}{2}\right)\right|^2}{(\omega-\omega_0)^2 + \left(\frac{\gamma_0}{2}\right)^2} + T_{bg}$$

Here, T_{bg} is a constant offset plus a linear background ($T_{bg} = B + C(\omega - \omega_0)$), A is the resonance amplitude, ω denotes the frequency of light while ω_0 is the resonant frequency, γ_0 is the damping constant. Δ denotes the Fano phase, and the Fano asymmetry parameter q is related to the Fano phase Δ as $q =$ -cot(Δ).[2] The quality factors are calculated as $Q = \frac{\omega_0}{\gamma_0}$.

2. Field profile of the high-Q mode in the pillar array

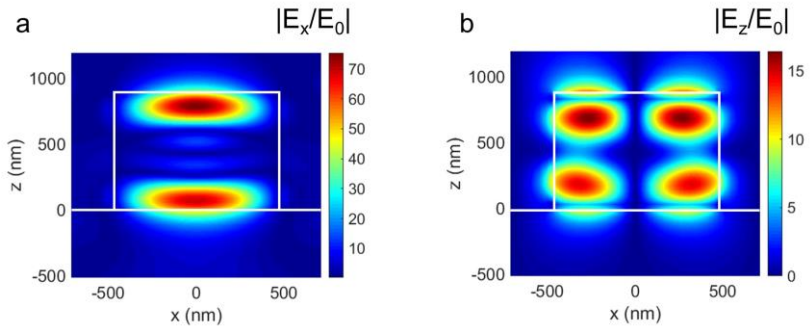


Figure S1. Spatial distribution of the electric field amplitude inside the metasurface unit cell shown in Figure 1, which described the case of an array of a-Si pillars on an SiO_2 substrate. Namely, the length and width of the pillar are taken to be $l = w = 963$ nm. The metasurface period is $P_x = P_y =$ 1425 nm. The electric field is plotted in the *x*-*z* plane, which goes through the center of the pillar (the same as in Figure 1d). a) *x*-component of the electric field, b) *z*-component of the electric

field. Field profiles are plotted at a resonant wavelength of the resonance dip shown in Figure 1c. The E_y component is identically equal to zero ($E_y = 0$).

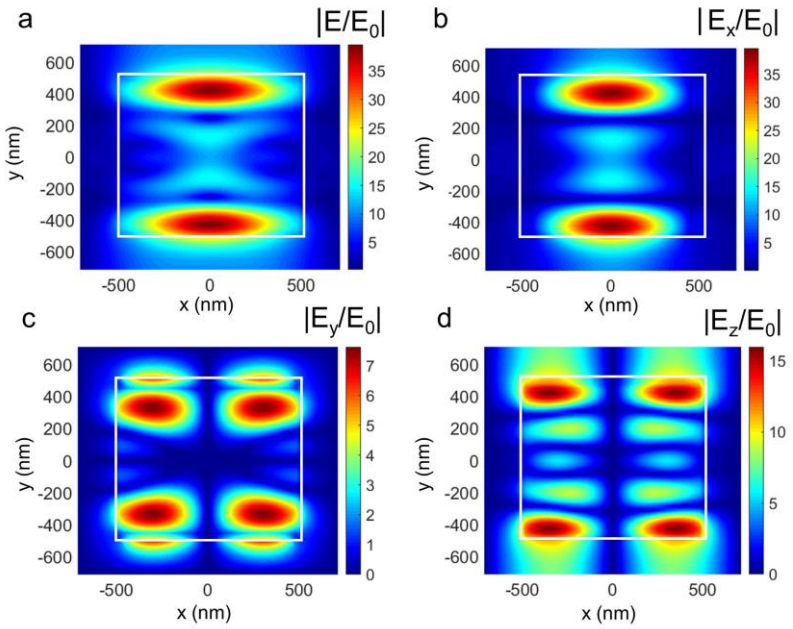


Figure S2. Spatial distribution of the electric field amplitude inside the metasurface unit cell shown in Figure 1, which described the case of an array of a-Si pillars on an SiO_2 substrate. The length and width of the pillar are taken to be $l = w = 963$ nm. The metasurface period is $P_x = P_y = 1425$ nm. The electric field is plotted in the x-y plane, which goes through the center of the pillar. a) An absolute value of the electric field, b) x-component of the electric field, c) y-component of the electric field, d) z-component of the electric field.

3. Optical response of a pillar array: effect of the pillar height on the array performance

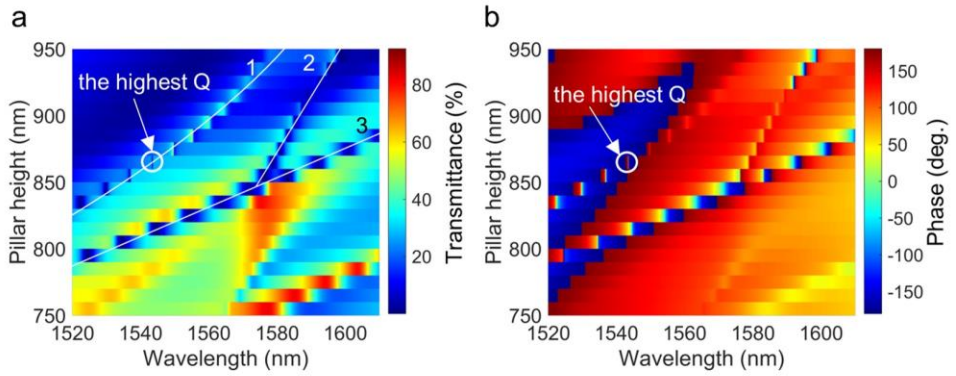


Figure S3. Optical response of a-Si pillar array on an SiO_2 substrate. The metasurface design is the same as in Figure 1 and 2. Namely, the length and width of the pillar are taken to be $l = w = 963$ nm. The metasurface period is $P_x = P_y = 1425$ nm. Transmittance a) and the phase of a transmitted

light b) as a function of wavelength and the a-Si pillar height *h*. We observe that modes 2 and 3 coalesce at a pillar height of *h* = 850 nm, and the highest-Q high-Q mode is observed at a pillar height of *h* = 860 nm.

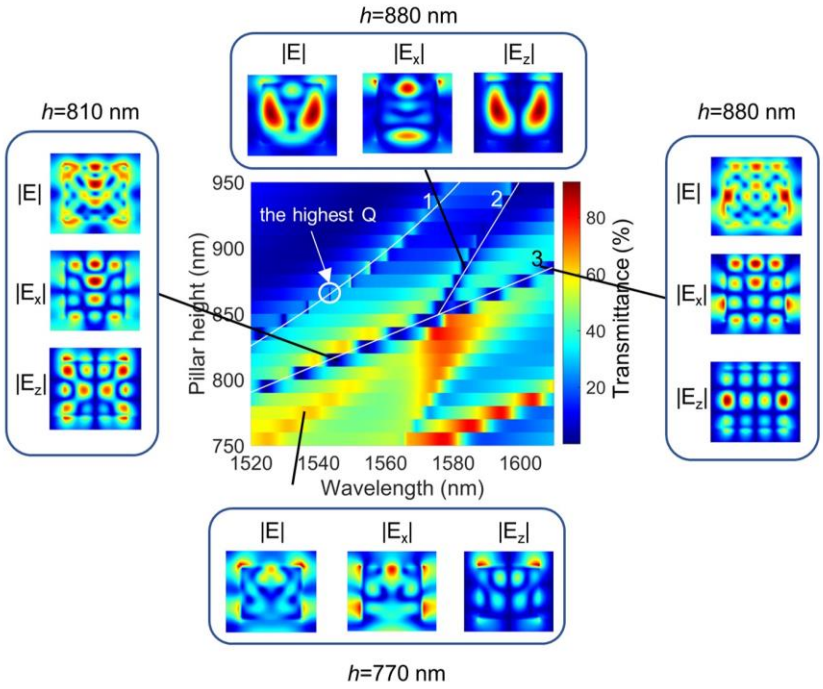


Figure S4. Spatial electric field profiles of a lower Q modes supported by the metasurface in the ***x*-*z* plane**, which passes through the center of the pillar. In the displayed electric field profiles, the *z* coordinate ranges from *z* = -200 nm to *z* = 1000 nm while the top of the SiO_2 substrate corresponds to the plane *z* = 0. The *x* coordinate ranges from *x* = -712.5 to *x* = 712.5 nm. The displayed false color plot is identical to Figure S3a. The spatial field profile of the high-Q mode is identical to the one shown in Figure 1, S1, and S2. We observe that *x*- and *y*-components of the electric field of mode 3 have very similar features when varying the pillar height. On the other hand, mode 2 'disappears' after coalescing with mode 3. The mode profile of mode 1 is identical to the one shown in Figure 1, and S1.

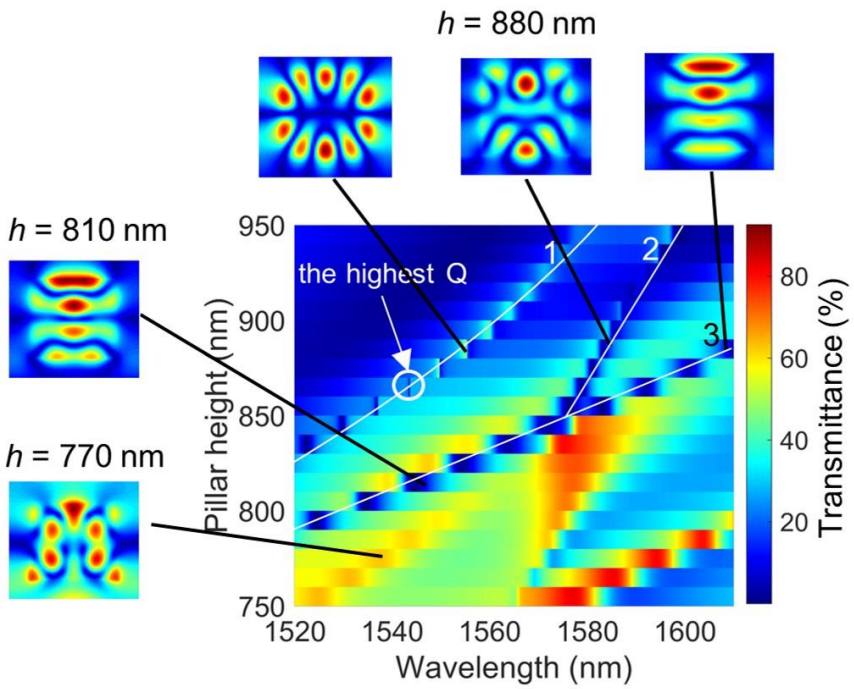


Figure S5. Spatial electric field profiles of a lower Q modes supported by the metasurface in the ***y-z* plane**, which passes through the center of the pillar. In the displayed electric field profiles, the *z* coordinate ranges from *z* = -200 nm to *z* = 1000 nm while the top of the SiO_2 substrate corresponds to the plane *z* = 0. The *x* coordinate ranges from *x* = -712.5 nm to *x* = 712.5 nm. The displayed false color plot is identical to Figure S3a. The spatial field profile of the high-Q mode is identical to the one shown in Figure 1, S1, and S2. We observe that *x*- and *y*-components of the electric field of mode 3 have very similar features when varying the pillar height. On the other hand, mode 2 'disappears' after coalescing with mode 3. The mode profile of mode 1 is identical to the one shown in Figure 1, and S1. In this Figure, we display electric field amplitude |*E*|. On the considered *y*-*z* plane, the only non-zero component is E_x.

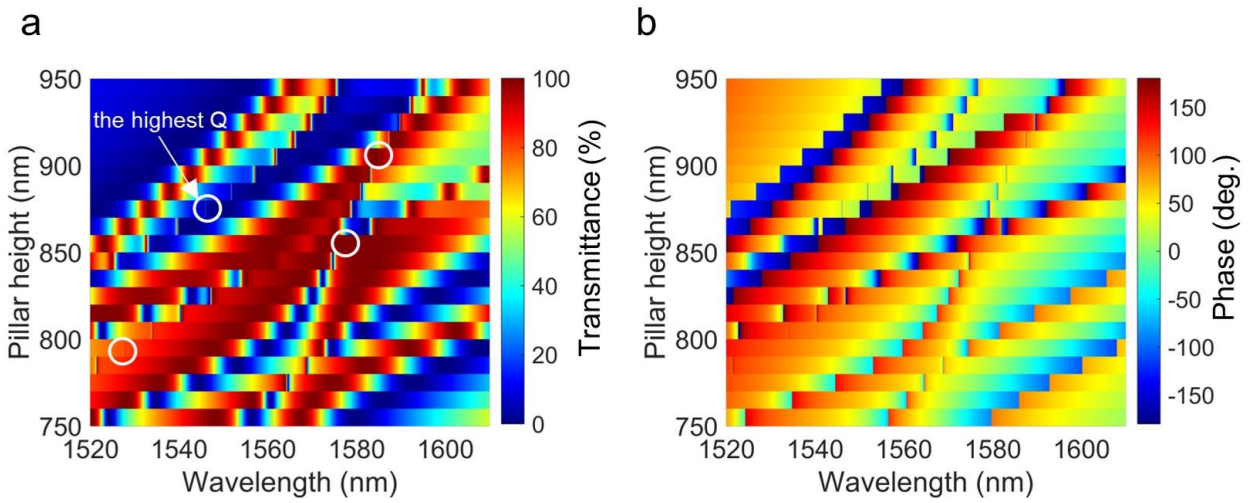


Figure S6. Optical response of a-Si pillar array suspended in air. The assumed geometrical parameters are the same as in Figure 1. Namely, the length and width of the pillar are taken to be $l = w = 963$ nm. The metasurface period is $P_x = P_y = 1425$ nm. In a), the transmittance as a function of wavelength and the a-Si pillar height h. In b), the phase of the transmitted light as a function of wavelength and the a-Si pillar height h. Compared with the case of pillars on an SiO_2 substrate, we observe the abundance of extremely high-Q modes, which are marked by a white circle in a). At the pillar height of $h = 870$ nm, the Q-factor of the observed high-Q mode is ~48,000.

When considering an a-Si pillar array we observe that at a pillar height of 870 nm, we are still able to couple to the resonant mode, and the resonant spectral feature is still visible from the false color plots of the transmittance and phase spectra (Figure S6). The extracted Q-factor of the resonance is ~48,000 (Figure S7a). In our simulation, we assumed a 5 nm mesh in z direction. Running a series of simulations with finer mesh could potentially enable us to identify the parameter values at which the mode with even higher Q-factor can be observed. We also observe that when take the metasurface period as $P_x = 1520$ nm and $P_y = 1425$ nm, the Q-factor of the supported mode is 221,000 (Figure S7b). Thus, increasing the metasurface period from $P_x = 1425$ nm to $P_x = 1520$ nm can strongly affect the quality factor of the metasurface.

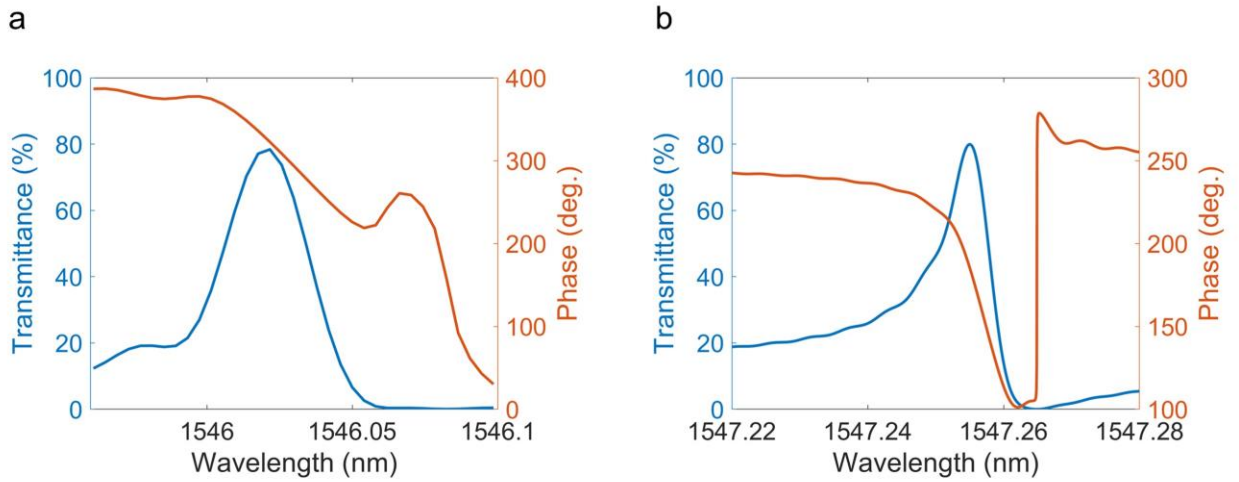


Figure S7. Transmittance and phase spectrum for an array of a-Si pillars *in air*. The assumed width, length and height of the pillars are $w = l = 963$ nm, $h = 870$ nm (see the schematic in Figure 1). In a), the values for the period are $P_x = 1425$ nm and $P_y = 1425$ nm. The extracted Q-factor of the resonance is ~48,000. The mesh is 20 nm in the *x*- and *y*-directions, and 5 nm in the *z*-direction. In b), the values for the period are as compared with a). In b), $P_x = 1520$ nm and $P_y = 1425$ nm. To reduce simulation time, we assumed a mesh of 20 nm in all three directions. The extracted Q-factor of the resonance is ~211,000.

4. Optical response of a pillar array: effect of the pillar period on the array performance

We study how the period of the metasurface affects the modes supported by the metasurface consisting of an array of a-Si pillars on an SiO_2 substrate (Figure 1). For metasurface periods exceeding 1200 nm, we observe three distinct modes in the transmittance and phase false color plots, which correspond to the high-Q mode at wavelength around 1540 nm and two lower-Q modes at wavelengths around 1580 nm and 1590 nm, which correspond to mode 2 and mode 3 from Figure S3. When studying the dependence of the mode position on the *x*-period P_x, we observe that the quality of the high-Q mode gradually increases with period (Figure S8c and S9c). We also observe that for periods of $P_x > 1300$ nm, the position of the high-Q mode is does not change significantly with period. We also observe that mode 2 shifts stronger with the *x*-period P_x as compared with mode 3. We also observe, that when we change the *y*-period P_y, the high-Q mode shifts stronger as compared with the case when the *y*-period is changed (c.f. Figure S8c and S9c). This result is also consistent with the

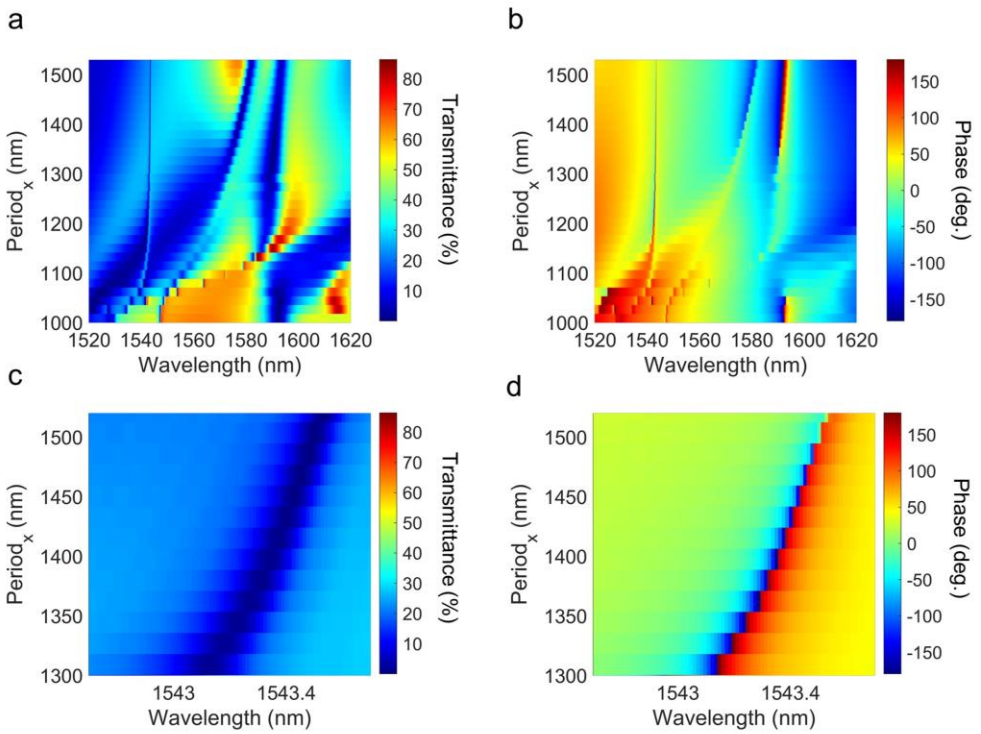


Figure S8. Optical response of an a-Si pillar array on an SiO_2 substrate when the incoming electric field is *x*-polarized (see Figure 1). The metasurface design is the same as in Figure 1 and 2. Namely, the length and width of the pillar are taken to be $l = w = 963$ nm, the height of the pillar is $h = 860$ nm. The metasurface period in the *y*-direction is $P_y = 1425$ nm. Transmittance a) and the phase of a transmitted light b) as a function of wavelength and the period in the *x*-direction P_x. c) and d) take a closer look at the behavior of the high-Q mode by limiting the range of the *x*-period to [1300 nm, 1520 nm] in a) and b), respectively. In c) and d), the wavelength range is limited to [1542.7 nm, 1543.7 nm].

specifics of the spatial mode profiles of the high-Q mode in the *x*-*z* and *y*-*z* planes (see Figure 1). When the *y*-period P_y increases from 1300 nm to 1520 nm, the high-Q resonance position shifts by ~5 nm.

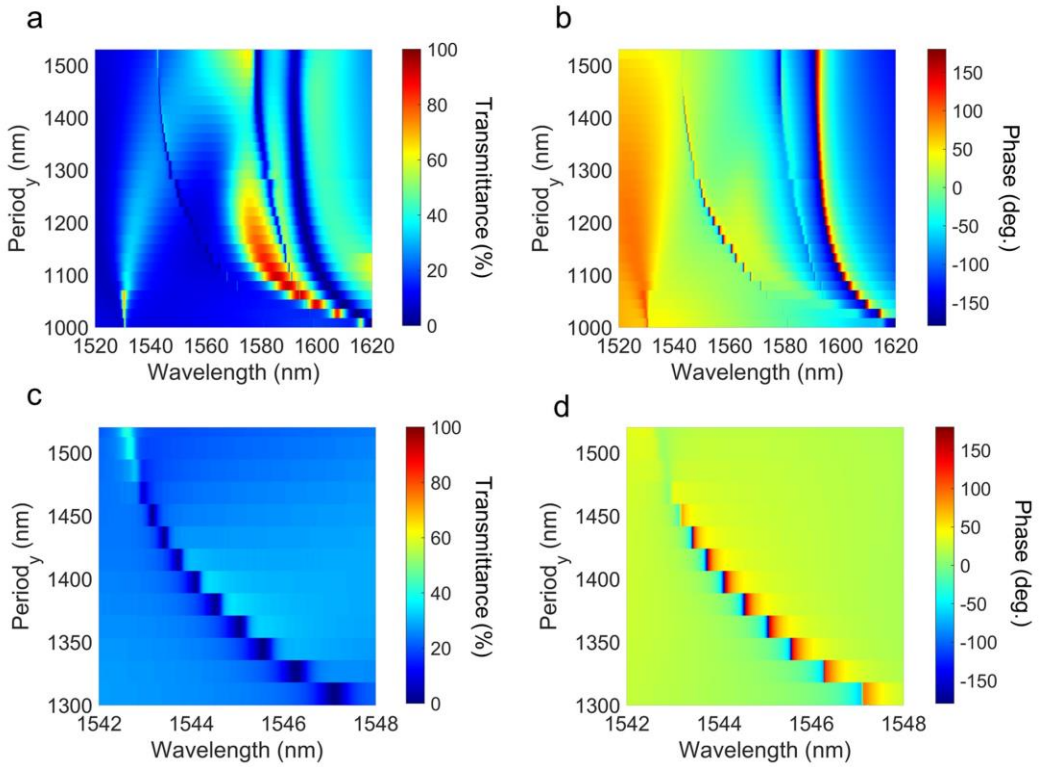


Figure S9. Optical response of an a-Si pillar array on an SiO_2 substrate when the incoming electric field is *x*-polarized (see Figure 1). The metasurface design is the same as in Figure 1 and 2. Namely, the length and width of the pillar are taken to be $l = w = 963$ nm, the height of the pillar is $h = 860$ nm. The metasurface period in the *x*-direction is $P_x = 1425$ nm. Transmittance a) and the phase of a transmitted light b) as a function of wavelength and the period in the *y*-direction P_y. c) and d) take a closer look at the behavior of the high-Q mode by limiting the range of the *y*-period to [1300 nm, 1520 nm] in a) and b), respectively. In c) and d), the wavelength range is limited to [1542 nm, 1548 nm].

5. Modes supported by a single isolated pillar

So far, in our optical simulations we imposed periodic boundaries in x- and y- directions implying that we investigate a periodic array of square a-Si pillars. It is not clear whether the identified photonic mode is also supported by an isolated a-Si pillar. To address this question, we simulate scattering cross section of an isolated pillar. In the revised simulation, we use perfectly matched layer (PML) boundary conditions at all simulation boundaries. First, we consider the case of a *single a-Si pillar in air* and calculate its scattering cross section as a function of wavelength and

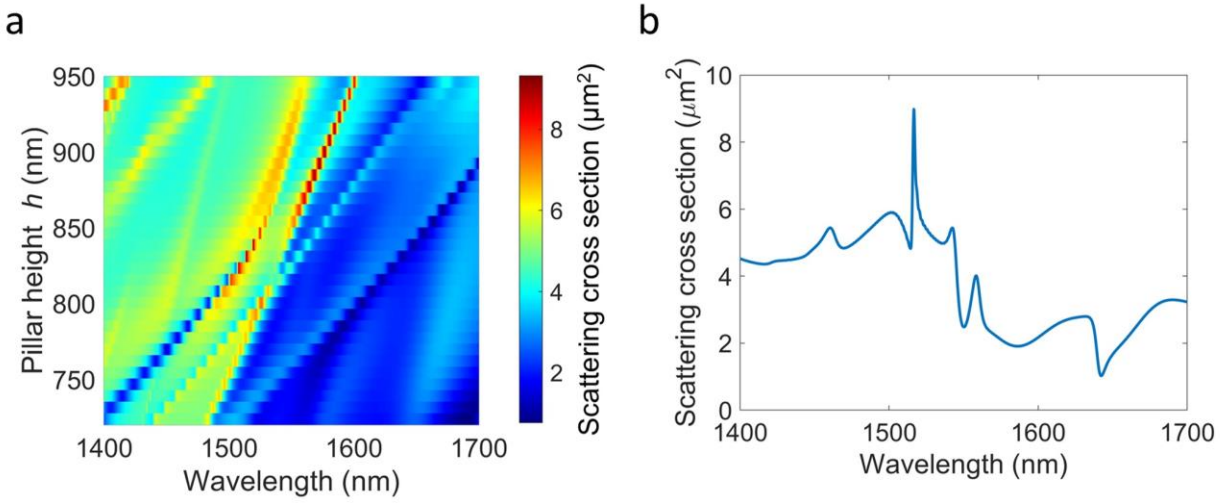


Figure S10. a) Scattering cross section of a single a-Si pillar *in air* as a function of wavelength and pillar height. The length and width of the pillar is $l = w = 963$ nm. b) Scattering cross section of a single a-Si pillar in the air where the pillar height is $h = 834$ nm. The highest-Q mode is observed at a wavelength of $\lambda = 1519.8$ nm.

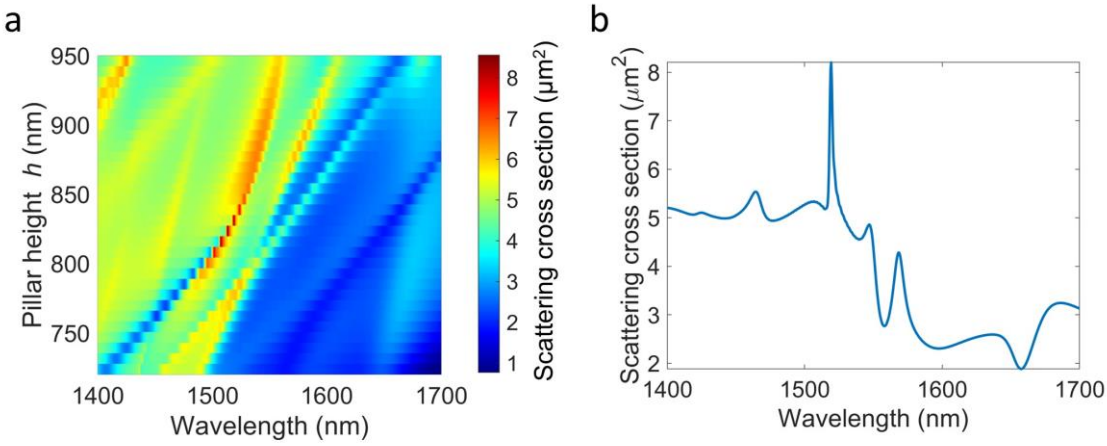


Figure S11. a) Scattering cross section of a single a-Si pillar on an SiO_2 *substrate* as a function of wavelength and pillar height. The length and width of the pillar is $l = w = 963$ nm. b) Scattering cross section of a single a-Si pillar where the pillar height is $h = 830$ nm. The highest-Q mode is observed at a wavelength of $\lambda = 1519.2$ nm.

pillar height (Figure S10a). The length and width of the pillar are the same as in Figure 1 of the main manuscript ($l = w = 963$ nm). As seen in Figure S10, in the vicinity of the highest-Q mode

we also observe crossing of two other modes. For a pillar height of h = 834 nm, the quality factor of the highest-Q mode is ~1000.

Next, we study the case of an isolated a-Si pillar on an SiO_2 substrate. Figure S11 plots the scattering cross section of an isolated pillar on an SiO_2 substrate as a function of wavelength and pillar height (Figure S11a). We observe an overall broadening of the spectral features as compared with the case of a single a-Si pillar in the air. We also observe that for a pillar height of 830 nm, the Q-factor of the supported mode is 676.

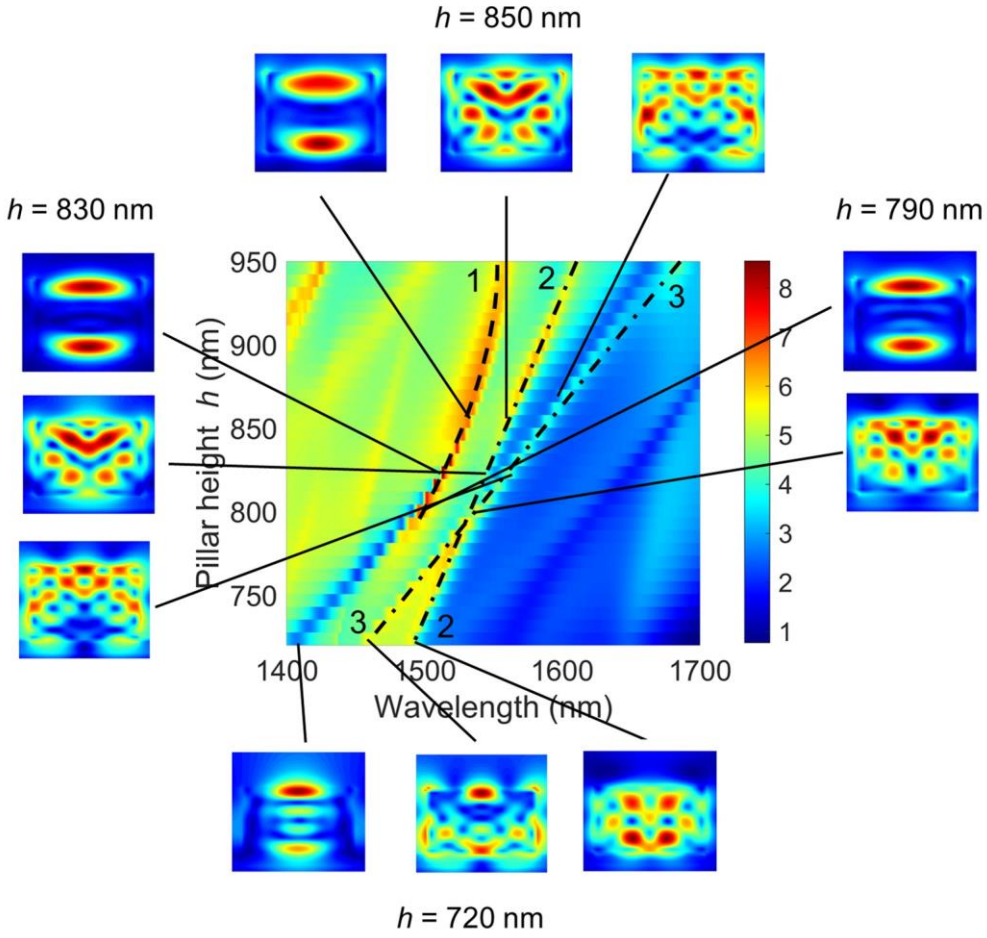


Figure S12. Scattering cross section of a single a-Si pillar on an SiO_2 substrate as a function of wavelength and pillar height (the same as Figure S11a). We plot the spatial distribution of the electric field amplitude $|E|$ in the a-Si pillar for the pillar heights of h = 720 nm, h = 790 nm, h = 830 nm, and h = 850 nm. The electric field is plotted in the x-z plane, which passes through the center of the pillar. The solid black lines point towards the scattering peaks at which the field profiles have been simulated.

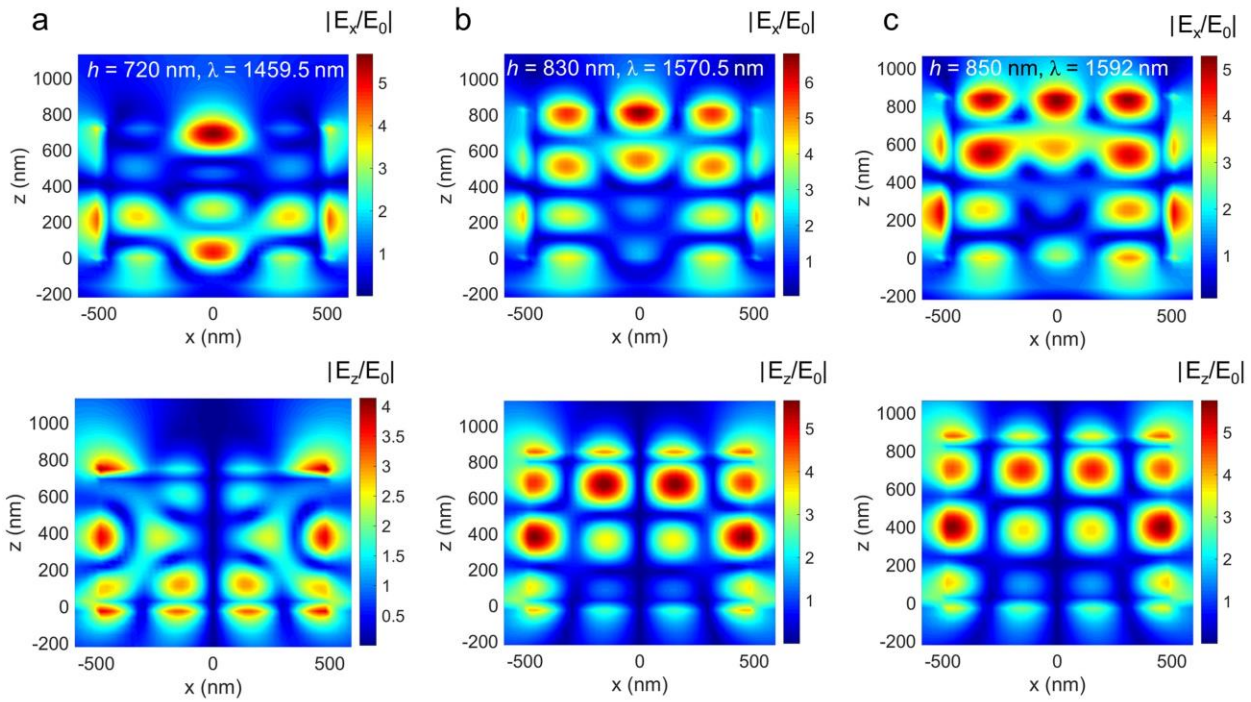


Figure S13. Spatial distribution of the *x*-component (top panel) and *y*-component (bottom panel) of the electric field **E** in the *x*-*z* plane, which passes through the center of an isolated a-Si pillar on an SiO_2 substrate. The *x*- and *z*- components of the electric field are plotted along the *modal line 3* in Figure S10. Geometrical parameters of the pillar are the same as in Figure S10. The a-Si pillar height and the operating wavelength are marked at the top of each column. We observe that the *x*- and *z*- components of the electric field gradually change as we increase the pillar height.

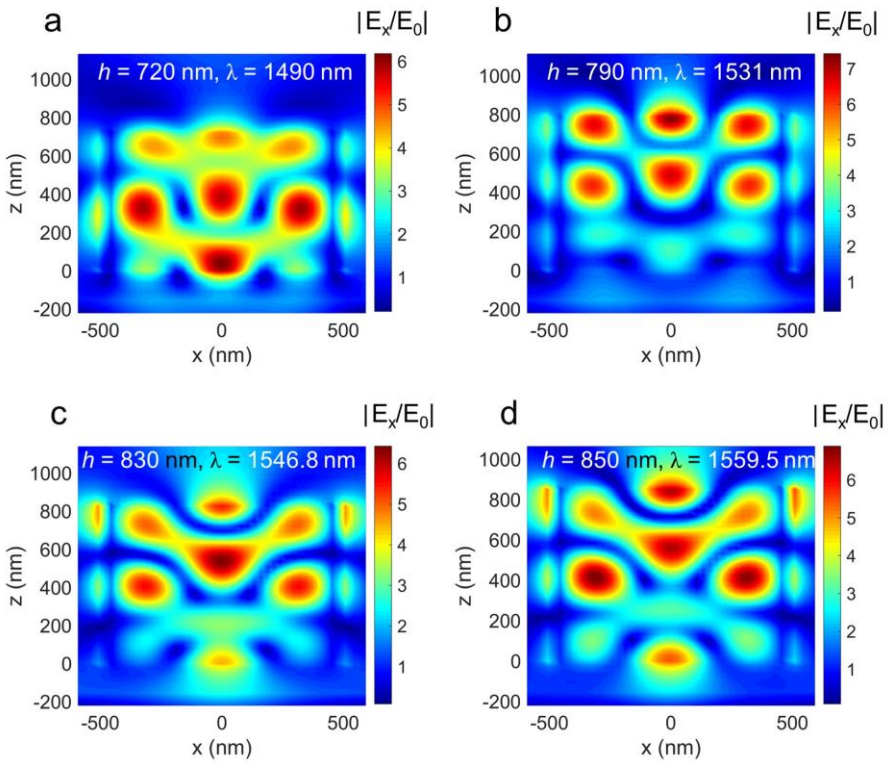


Figure S14. Spatial distribution of the *x*-component of the electric field **E** in the *x*-*z* plane, which passes through the center of an isolated a-Si pillar on an SiO_2 substrate. The *x*-component of the electric field is plotted along the *modal line 2* in Figure S10. Geometrical parameters of the pillar are the same as in Figure S10. The a-Si pillar height and the operating wavelength are marked at the top of each column. We observe that the *x*-components of the electric field gradually changes as we increase the pillar height.

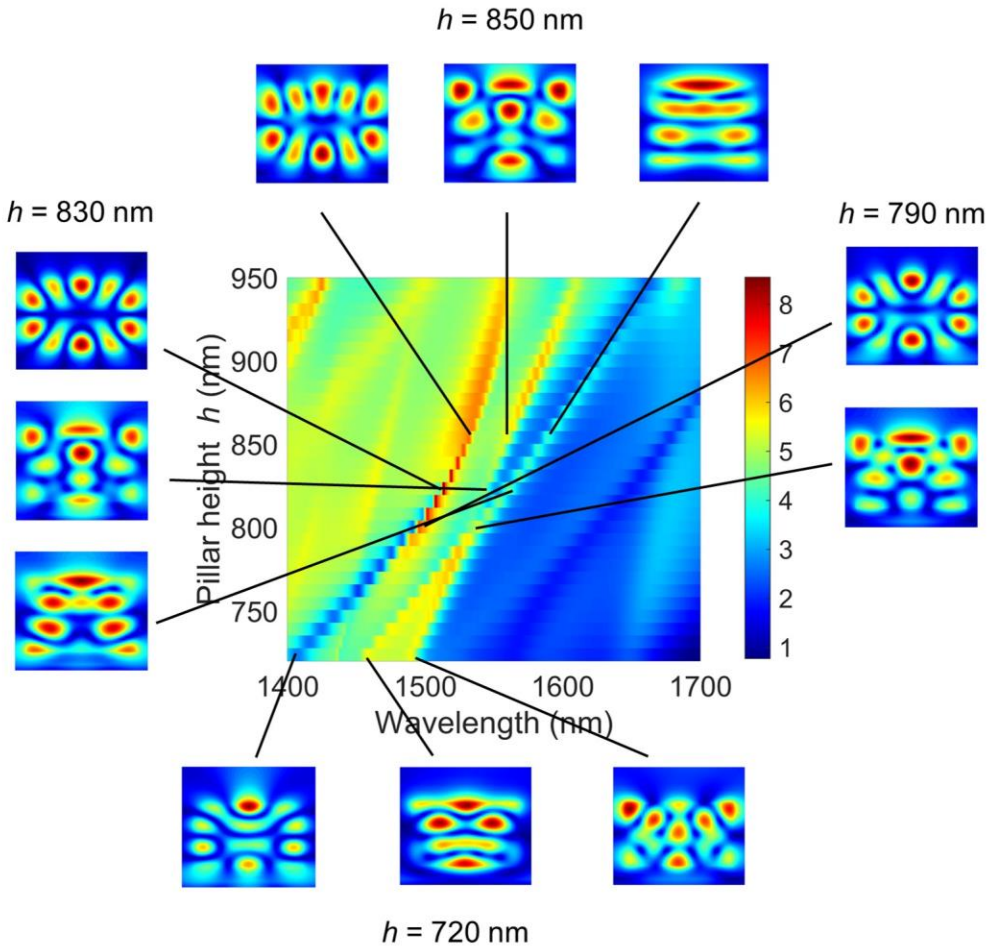


Figure S15. Scattering cross section of a single a-Si pillar on an SiO_2 substrate as a function of wavelength and pillar height (the same as Figure S11a). We plot the spatial distribution of the electric field amplitude |E| in the a-Si pillar for the pillar heights of h = 720 nm, h = 790 nm, h = 830 nm, and h = 850 nm. The electric field is plotted in the y-z plane, which passes through the center of the pillar. The solid black lines point towards the scattering peaks at which the field profiles have been simulated.

To understand the nature of the considered high-Q resonance and its relation to the high-Q resonance observed in the case of an array, we display the spatial distribution of the electric field amplitude in the y-z cross-section of the resonator (Figure S15). As seen in Figure S15, the spatial distribution of the electric field amplitude of the high-Q mode in the y-z plane (for example, at h = 830 nm) is identical to the spatial distribution of the electric field observed in the case of the pillar array (see Figure 1e).

6. Controlling the spectral shape of the resonance

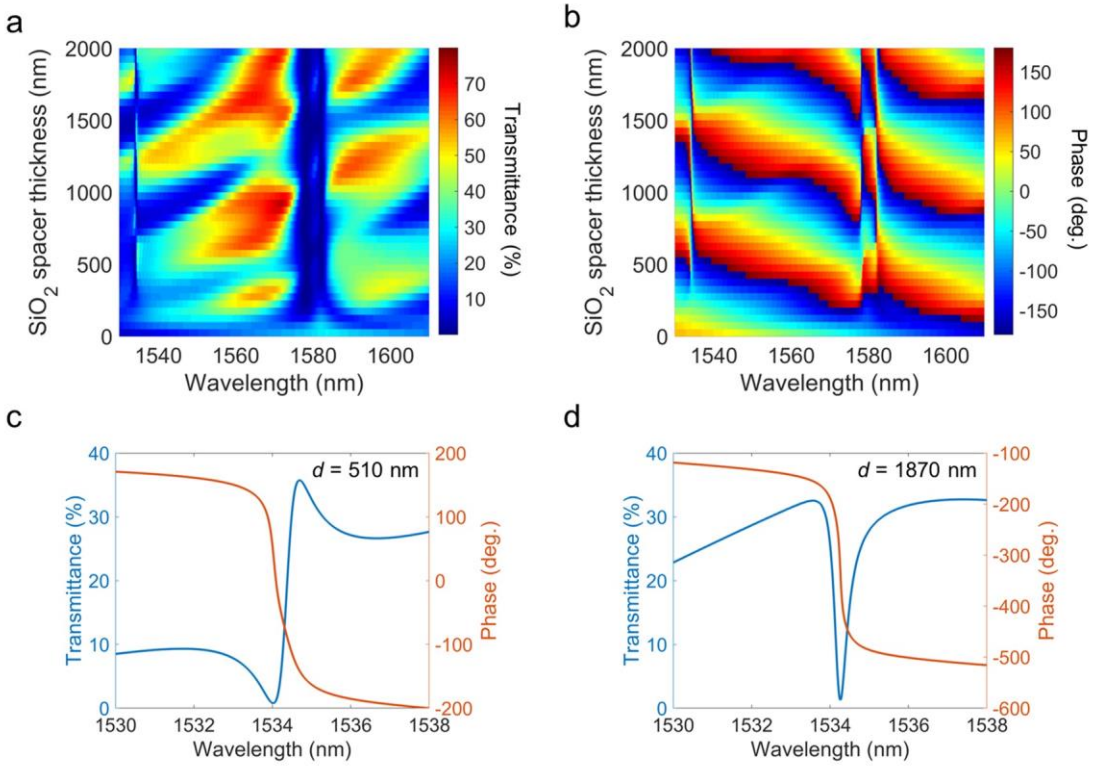


Figure S16. Transmittance a) and phase of the transmitted light b) as a function of the wavelength and thickness of the SiO_2 spacer d (see the schematic in Figure 3a). The assumed geometrical parameters are the same as in Figure 3. c) and d) show transmittance and phase spectra for the SiO_2 spacer thickness for d = 510 nm and d = 1870 nm.

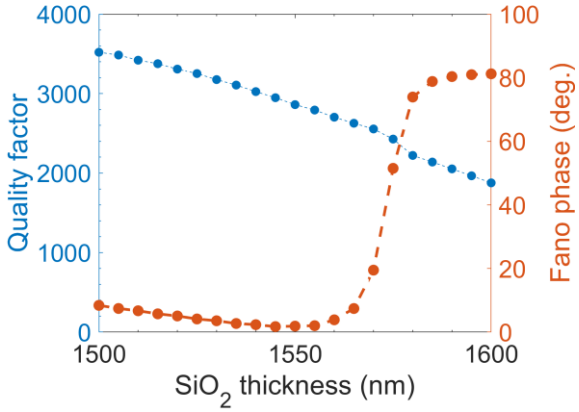


Figure S17. Quality factor and Fano phase of the high-Q resonance as a function of the SiO_2 thickness d (for schematic see Figure 3a). Here, the considered structure and geometrical parameters are identical to the one if Figure 3. Figure 3c shows that around the SiO_2 spacer

thickness d = 1550 nm, the Fano phase varies abruptly as a function of the SiO_2 spacer thickness. Here, we sample the SiO_2 spacer thickness more finely to accurately capture the details of the variation of the Fano phase.

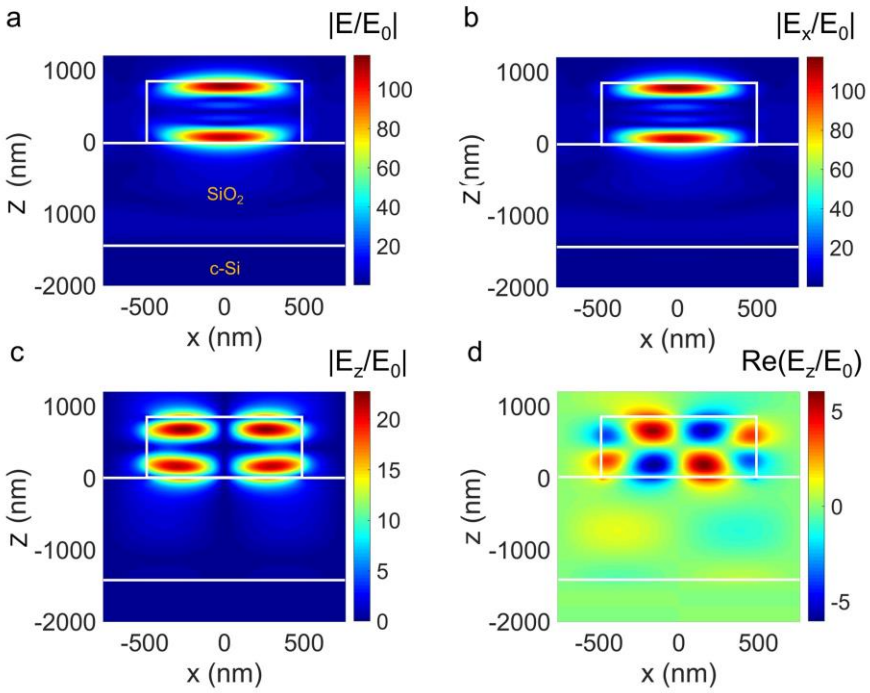


Figure S18. Spatial distribution of the electric field amplitude in the metasurface unit cell depicted in Figure 3a. The geometrical parameters of the metasurface unit cell are as follows: the length and width of the pillar is $l = w$ = 963 nm, the height of the pillar is h = 845 nm. The assumed period values are P_x = 1520 nm and P_y = 1425 nm. The thickness of the SiO_2 spacer is d = 1450 nm. The spatial distribution of the electric field is plotted in the x-y plane. In a), we plot the absolute value of the electric field $|E/E_0|$. In b) and c), we plot the spatial distributions of x- and z-components of the electric field, respectively. In d), we plot the real part of the z-component of the electric field. We observe that both x- and z-components of the electric filed adopt non-zero values in the SiO_2 spacer.

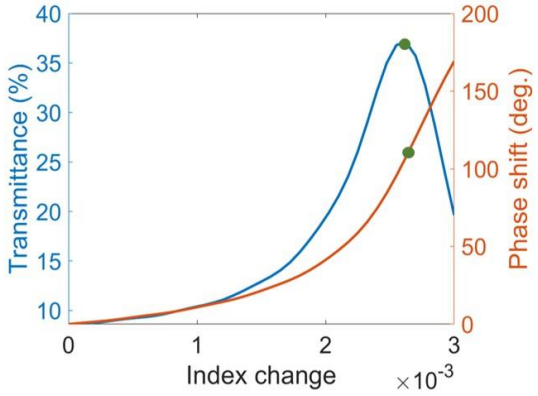


Figure S19. Transmittance and phase shift as a function of the a-Si index change achieved by using a high-Q resonance shown in Figure 3b. The wavelength is fixed at an operating wavelength $\lambda = 1535.44$ nm at which we have been able to fully suppress the first diffraction order (Figure 3e). At an operating wavelength and for an index change of $\Delta n = 0.0026$, the phase shift extracted from a periodic array calculations is 107°.

7. Realistic electrical addressing architectures

In the present section, we describe how the proposed metasurface design can be modified to enable thermo-optic control of the wavefront of the transmitted light. The first variant of the proposed metasurface unit cell features a-Si pillars, which are connected via an a-Si bar (for a schematic of the unit cell see Figure S20a). In Figure S20a, the whole a-Si layer is lightly doped and is placed on an SiO_2 substrate so that the complex refractive index of a-Si now reads as $n = 3.734+0.0013$ i. We can actively control the temperature of the metasurface pixel by biasing the metasurface unit cell at the edge and flowing current in the y direction. the geometrical parameters of the proposed metasurface unit cell are as follows: $\delta = 82$ nm, $w = l_1 = 963$ nm, $h = 850$ nm, $P_x = P_y = 1500$ nm. The inset of Figure S20b shows a schematic of one period of a two-level phase grating, which is utilized to theoretically demonstrate switchable diffraction. Within a grating period, the assumed index change between neighboring a-Si pillars is $\Delta n=0.006$ (Figure S20b and S20a). The switchable diffraction is observed both in the case when the polarization of the electric field is perpendicular and parallel to the a-Si bars (Figure S20b and S20c, respectively). In Figure S20b, the operating wavelength is 1586.5 nm, and the overall transmittance at the operating wavelength is $T = 1.2\%$. In Figure S20c, the operating wavelength is 1583.2 nm, and the overall transmittance at the operating wavelength is $T=0.3\%$. Note that to observe the diffractive switching, we have utilized the lower-Q mode described in Figure 3 of the main manuscript. When using the configuration shown in Figure S20a, we are not able to demonstrate diffractive beam switching using the higher-Q mode (see Figure 1 of the main manuscript) since the spectral characteristics of the high-Q mode are strongly affected by introduced optical losses. Namely, in

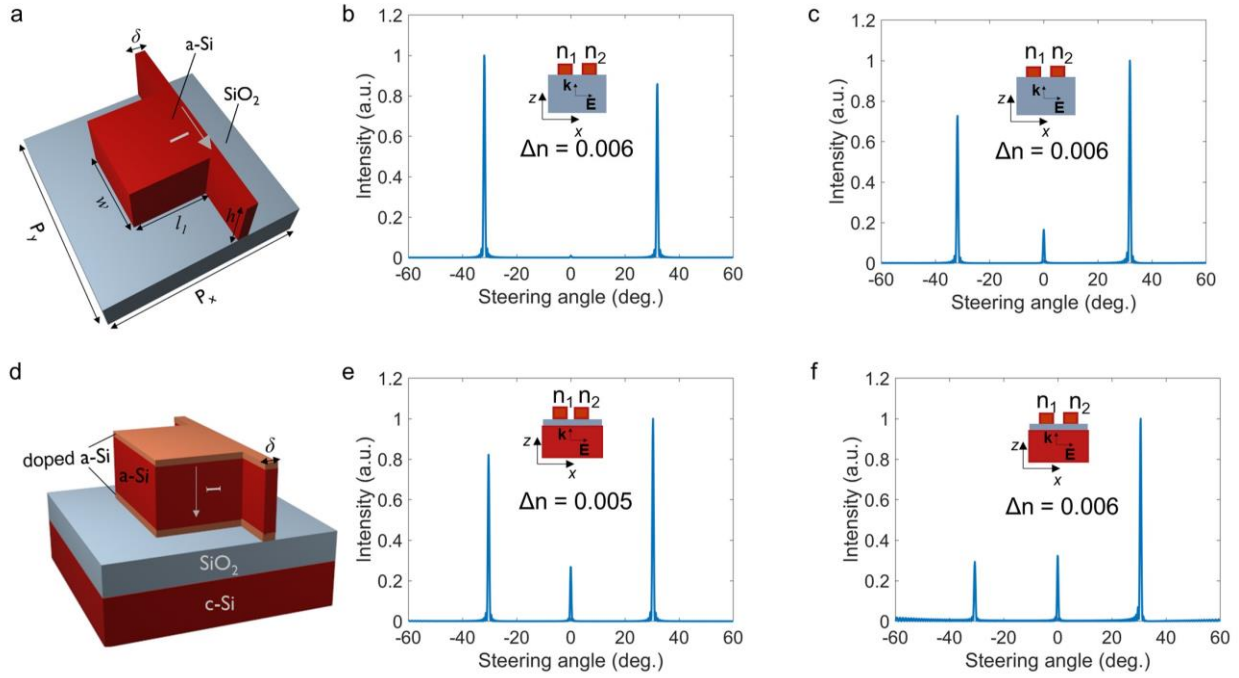


Figure S20. Dynamic beam switching with realistic interconnect architectures. a) Schematic of the proposed metasurface unit cell. The square a-Si pillars connected via a-Si bars. In a) the a-Si is lightly doped. b) and c) plot the electric field intensity in the far field as function of the steering angle for a two-level phase grating, which uses the unit cell shown in a). The a-Si refractive index difference between neighboring metasurface elements is Δn = 0.006. In b), the incoming plane wave is x-polarized while in c) the incoming electric field is y-polarized. d) Schematic of a metasurface unit cell in which the top and bottom 50 nm of a-Si are doped. The thickness of the SiO_2 layer is 1440 nm. e) and f) plot the electric field intensity in the far field as function of the steering angle for a two-level phase grating, which uses the unit cell shown in d). In e) the a-Si refractive index difference between neighboring metasurface elements is Δn = 0.005, and the width of the a-Si bar is δ = 40 nm. In f) the a-Si refractive index difference between neighboring metasurface elements is Δn = 0.006, and the width of the a-Si bar is δ = 82 nm.

the lossy structure (Figure S20a), we do not observe large spectral variation of the phase of the transmitted light in the case of no applied current.

To enable thermo-optic switching using also higher-Q mode we modify our metasurface unit cell design. In the modified unit cell design, only top and bottom 50 nm layers of the a-Si are doped while the core section of a-Si layer is practically undoped (or very lightly doped). In this implementation, the top and bottom electrodes are biased with respect to each other, and current flows in the vertical direction. We have also slightly modified the geometrical parameters of the metasurface unit cell. In S13d, P_x = 1520 nm and P_y = 1425 nm. The height of the a-Si and the a-Si bar is h = 845 nm, and the thickness of the SiO_2 spacer is 1440 nm. The width and length of the a-Si pillar are taken to be $w = l_1$ = 963 nm. The insets of Figure S20e and S20f show schematics of

one period of a two-level phase grating, which is utilized to theoretically demonstrate switchable diffraction. Utilizing the higher-Q mode, we have been able to observe switchable diffraction assuming that the refractive index difference between neighboring a-Si pillars in a grating period is $\Delta n = 0.005$, and the width of the a-Si bar of $\delta = 40$ nm. In Figure S20e, the polarization direction of the electric field of the incoming light is perpendicular to the a-Si bars. In Figure S20e, the operating wavelength is 1536.15 nm, while the overall transmittance at the operating wavelength is $T = 6.8$ %.

Interestingly, using the two-level phase grating, we have been able to observe highly asymmetric diffraction pattern originating from geometrical asymmetry of the proposed metasurface unit cell (Figure S20f). In Figure S20f, the refractive index difference between neighboring a-Si pillars in a grating period is $\Delta n = 0.006$. The width of the a-Si bar is taken to be $\delta = 82$ nm. the operating wavelength of the utilized lower-Q mode is 1548.4 nm, and the overall transmittance at the operating wavelength is $T = 1$ %.

Finally, we consider the case when the metasurface unit cells are placed on an SiO_2 pedestal and the a-Si pillars are connected in series vis a-Si bars. In this case, for the pillar height of h = 880 nm, the spectral and phase signatures of the high-Q mode are not observed.

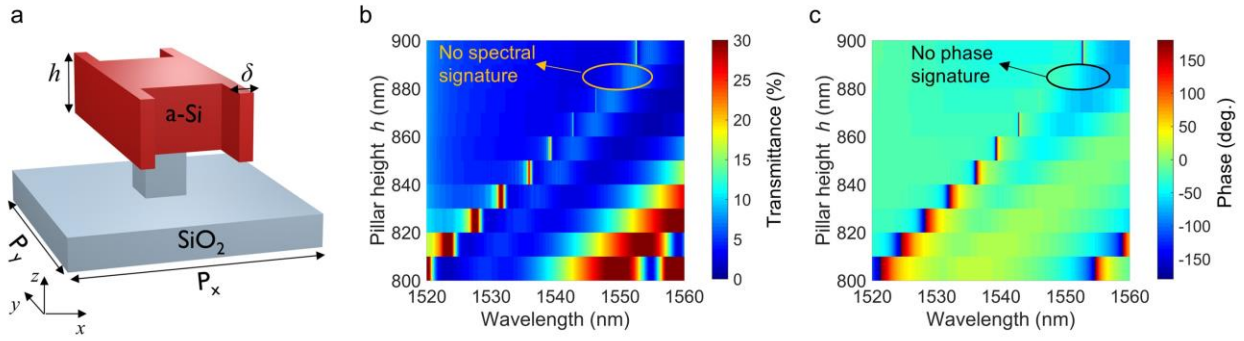


Figure S21. Dependence of the transmittance and phase on the height of the pillar and bars. a) Schematic of the metasurface unit cell. In the schematic, $P_x = 1520$ nm, $P_y = 1\,425$ nm, $\delta = 82$ nm. The height of the SiO_2 pedestal is 382 nm. The length of the pedestal is 200 nm, the width of the pedestal is also 200 nm. Note that the metasurface considered here does not include a Si substrate. In b), we plot transmittance as a function of wavelength and the a-Si pillar height. In c), we the phase of the transmitted light as a function of wavelength and the a-Si pillar height. When changing the height of the a-Si pillar, we simultaneously change the height of the a-Si bars. As seen in b) and d), at the pillar height of h = 880 nm, the spectral and phase signature of the resonance disappears.

The metasurface structure considered in the present section is shown in Figure 5a and 5b. The geometrical parameters of the considered structure are specified in the caption of Figure 5.

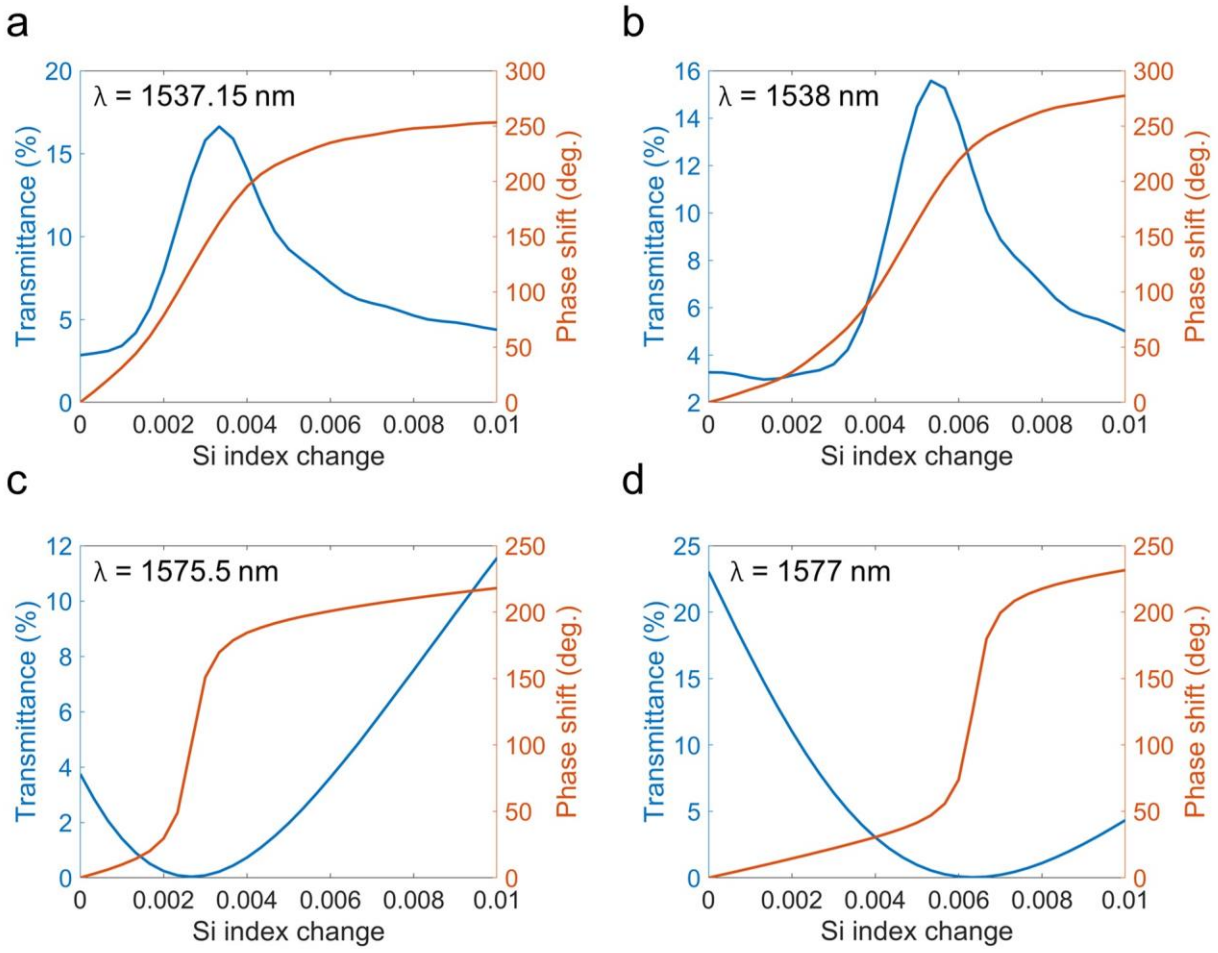


Figure S22. Transmittance and phase shift as function of the a-Si index change for the metasurface with electrodes shown in Figure 5a and 5b. The incoming light is *x*-polarized. a) and b) correspond to the high-Q high-Q mode while c) and d) correspond to the lower-Q mode. The maximal phase shift enabled by the high-Q high-Q mode is 277° while the lower-Q mode enables a phase shift of 230° when the refractive index of a-Si is changed by $\Delta n = 0.01$.

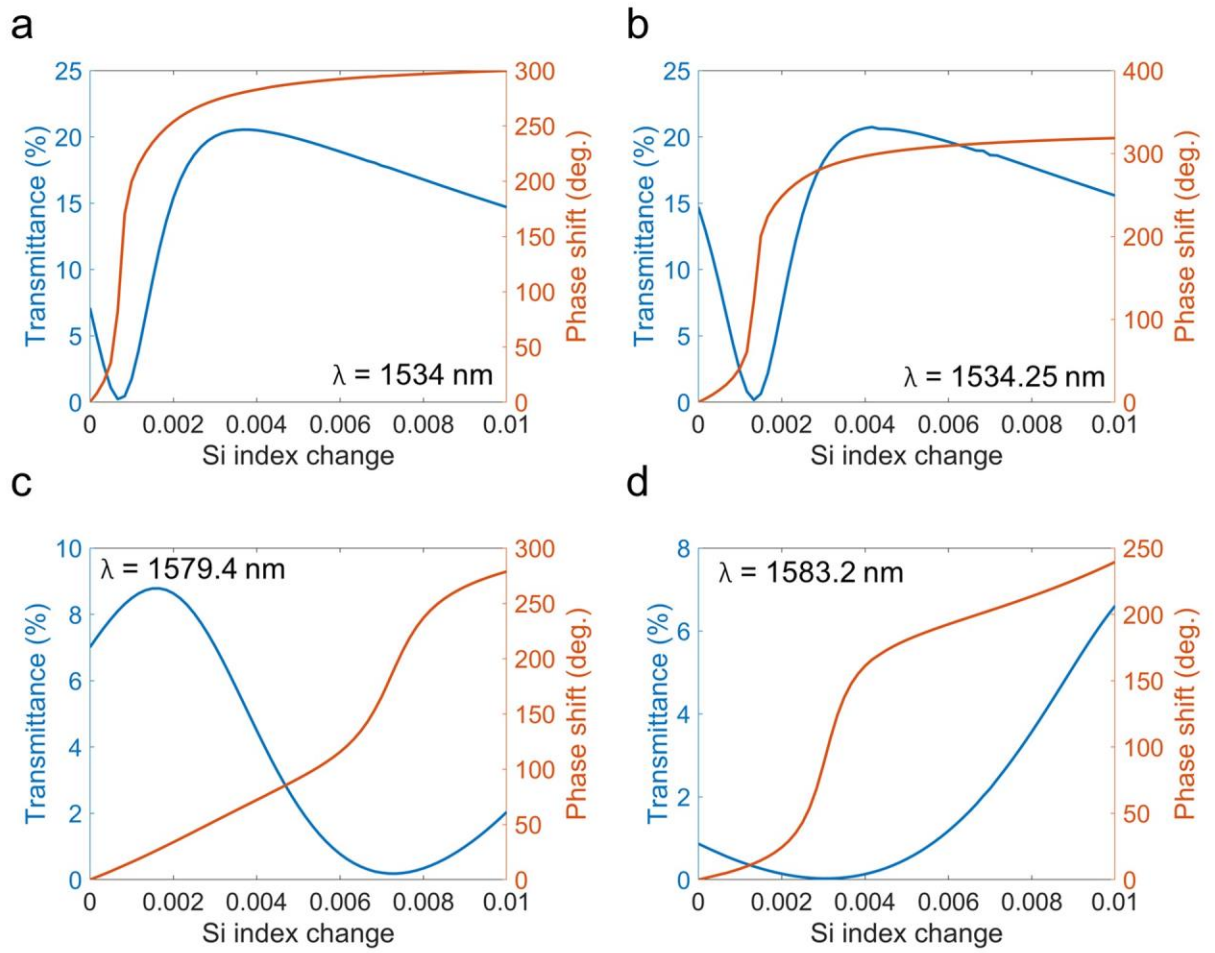


Figure S23. Transmittance and phase shift as function of the a-Si index change for the metasurface with electrodes shown in Figure 5a and 5b. The incoming light is *y*-polarized. a) and b) correspond to the high-Q high-Q mode while c) and d) correspond to the lower-Q mode. The maximal phase shift enabled by the high-Q high-Q mode is 320° while the lower-Q mode enables a phase shift of 275° when the refractive index of a-Si is changed by $\Delta n = 0.01$.

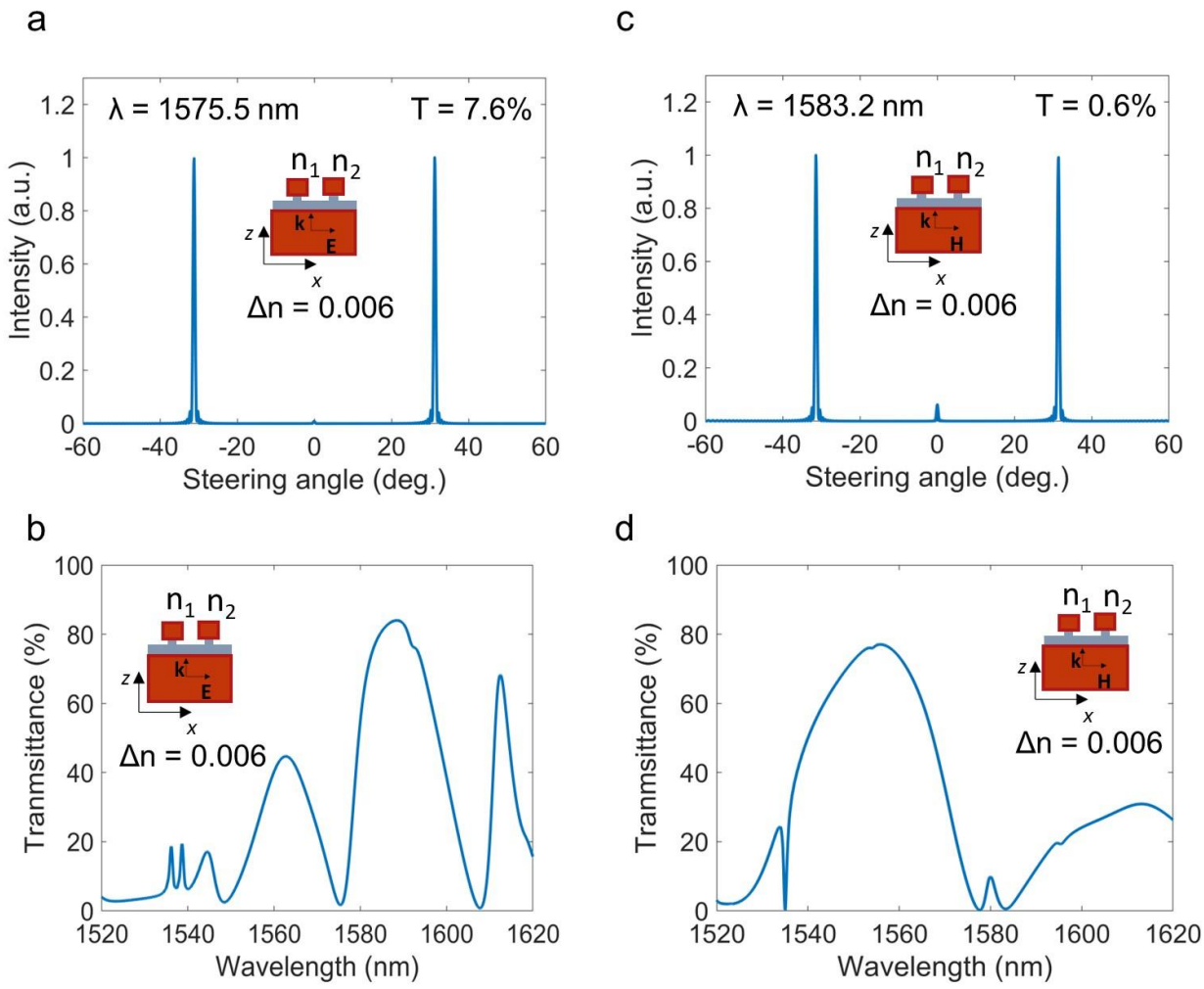


Figure S24. Thermo-optic beam switching using the lower-Q mode. The metasurface unit cell is given by the schematic shown in Figure 5a. We analyze the optical performance of a two-level phase grating. The unit cell of the grating is shown in the inset of a). The index change between neighboring a-Si pillars is $\Delta n = 0.006$. a) The intensity of the electric field in the far field when the incoming plane wave is x polarized, the operating wavelength is $\lambda = 1575.5$ nm, and the overall transmittance is T = 7.6 %. In b), the overall transmittance spectrum of the two-level grating studied in a). In c), The intensity of the electric field in the far field when the incoming plane wave is y polarized. In c), the operating wavelength is $\lambda = 1583.2$ nm, and the overall transmittance is T = 0.6 %. In d), the overall transmittance spectrum of the two-level grating studied in c).

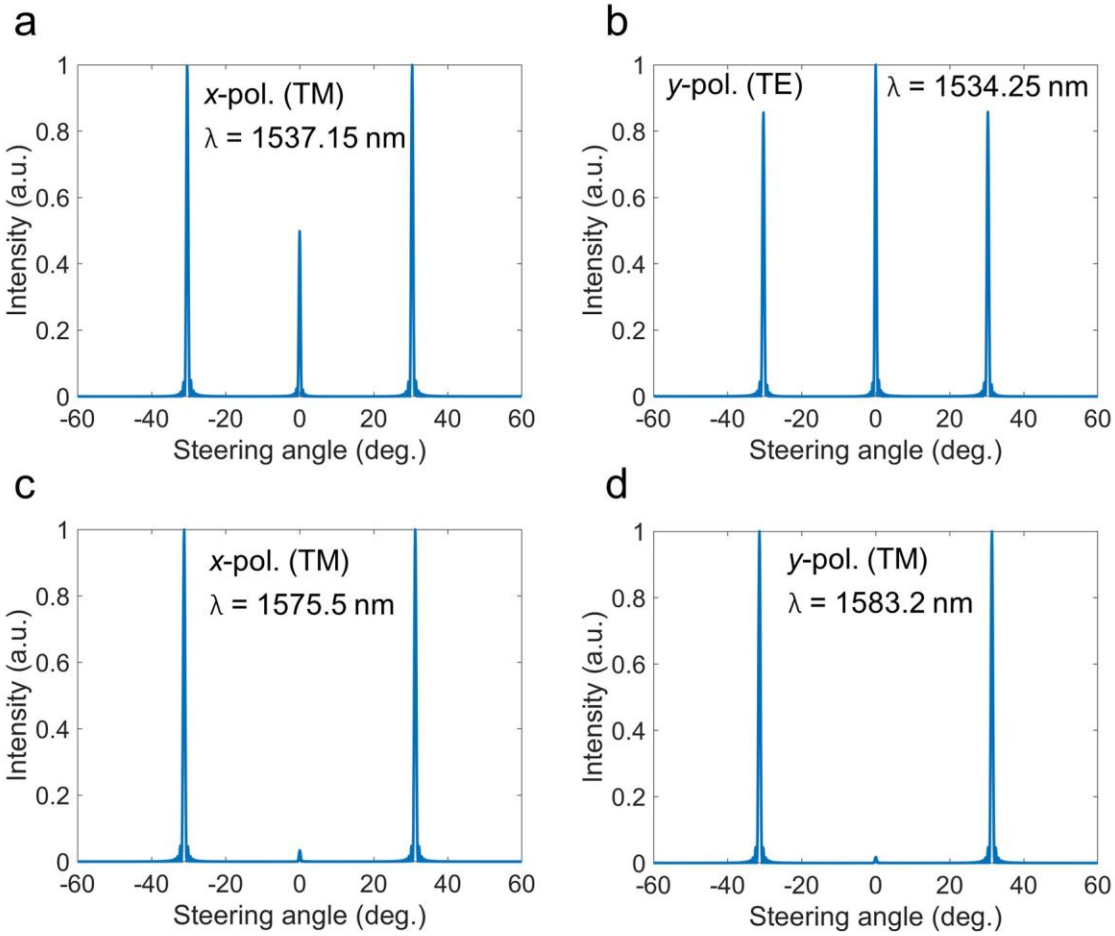


Figure S25. Analytical array factor calculations for a two-level phase grating.[3] The plots calculated intensity of the electric field in the far field as a function of the steering angle in the case of a two-level phase grating. a) and b) correspond to the case of the high-Q mode. In a) and b), we assume that the refractive index difference between neighboring metasurface pixels is 0.0026, which is the value chosen in Figure 5. In a) and b), the values of the electric field amplitudes and relative phases in a grating period are constructed based on Figure S22a and S23b. c) and d) correspond to the case of the lower-Q mode. In c) and d), we assume that the refractive index difference between neighboring metasurface pixels is 0.006, which is the value chosen in Figure S24. In c) and d), the values of the electric field amplitudes and relative phases in a grating period are constructed based on Figure S22c and S23d. We observe that, in the case of the high-Q mode, the array level analytical calculations yield significantly different results as compared with the case of full wave simulations providing evidence of near-field coupling between neighboring metasurface pixels [cf. c) and Figure 5c as well as d) and Figure 5e]. On the other hand, in the case of the lower-Q mode, the array factor calculation results and full wave simulations yield similar results (cf. c) and Figure S24a as well as d) and Figure S24).

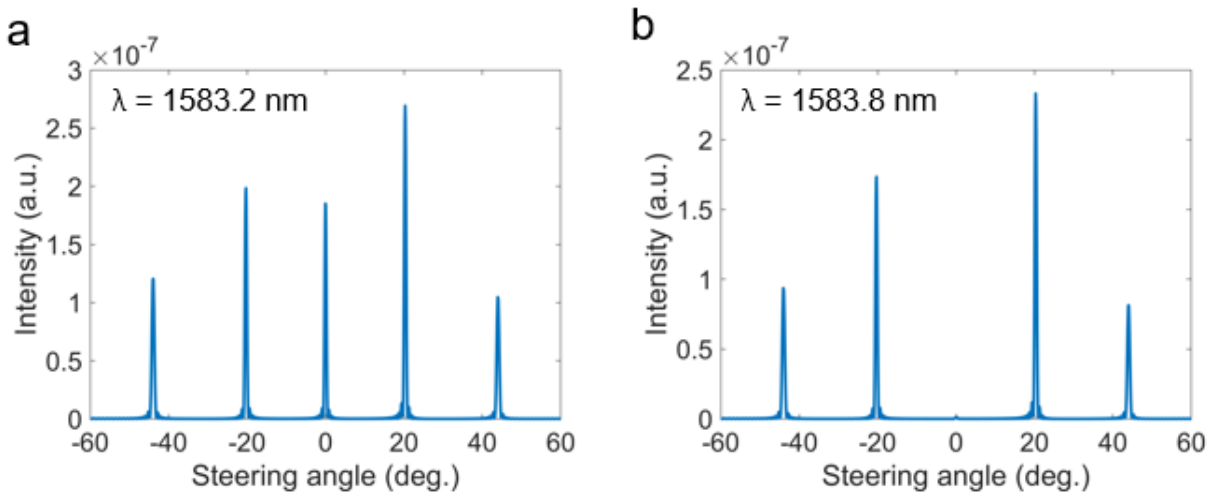


Figure S26. Intensity of the electric filed in the far field as a function of the steering angle in the cases of a three-level phase grating. The incoming light is *y*-polarized. The three-level phase grating is generated using the simulated phase shift data for an operating wavelength of λ = 1583.2 nm (Figure S23), and the phase shift values in the grating period are given as (0°, 120°, 240°). Within a grating period, the values of the real part of the refractive index are taken as (3.734, 3.734+0.003333, 3.734+0.01). a) plots the intensity of the electric field in the far field at an operating wavelength of λ = 1583.2 nm. In b), we keep the same spatial distribution of the real part of the refractive index as in a), but the operating wavelength is now taken as λ = 1583.8 nm. In a) we observe the target steered beam at a steering angle of 20.3°. Additionally, we observe a number of spurious diffraction orders. By changing the operating wavelength to λ = 1583.8 nm, we are able to fully suppress the zeroth diffraction order, but the other spurious diffraction orders are still observed.

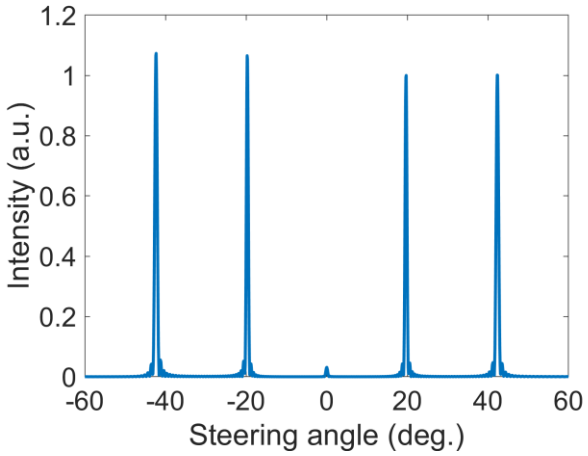


Figure S27. Intensity of the electric filed in the far field as a function of the steering angle in the cases of a three-level phase grating at an operating wavelength of λ = 1535.81 nm, which is a resonant wavelength for a high-Q mode. The incoming light is *y*-polarized. Within a grating period, the values of the real part of the refractive index are taken as (3.734, 3.734+0.003333, 3.734+0.01). By appropriately choosing the operating wavelength, we have been able to suppress the zeroth diffraction order.

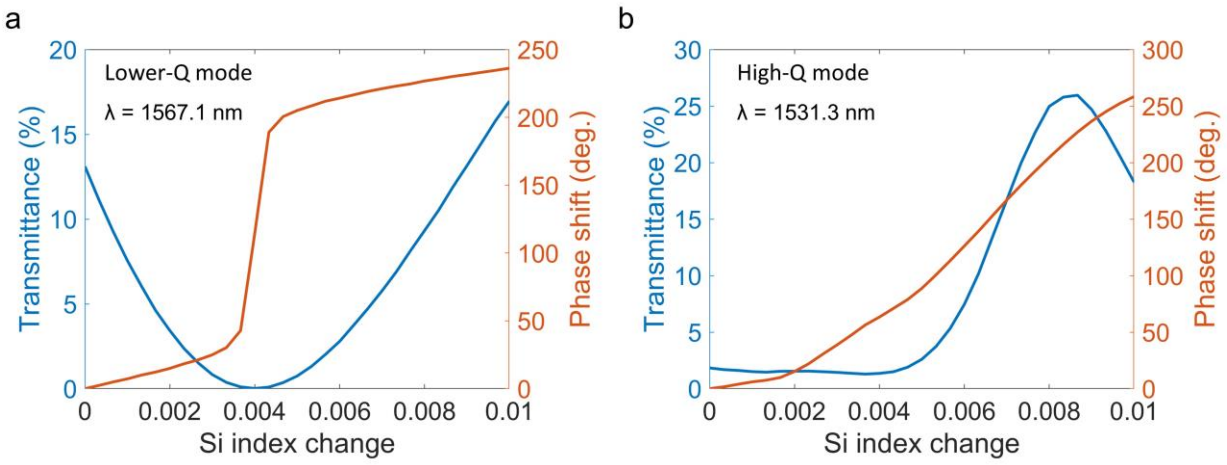


Figure S28. Transmittance and phase shift as function of the a-Si index change for an optimized metasurface with electrodes shown in Figure 5a and 5b. The incoming light is *x*-polarized. a) corresponds to the lower-Q mode and b) correspond to the high-Q mode. The insets indicate the operating wavelengths for which the diffraction patterns shown in Figure 7 are observed. At an operating wavelength of λ = 1567.1 nm, the maximal phase shift enabled by the lower-Q mode is 236.2°. In the case of the high-Q mode, the maximal phase shift at an operating wavelength of λ = 1531.3 nm is 265°.

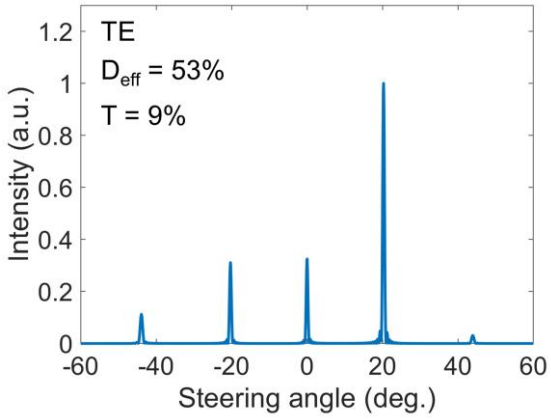


Figure S29. Thermo-optic three-level phase grating with a realistic interconnect architecture and optimized geometry. The incoming plane wave is TE-polarized. The figure plots the intensity of the electric field in the far field for the case of the lower-Q mode at an operating wavelength of λ = 1581.5 nm. The employed optimization procedure has yielded the following geometrical parameters for the structure shown in Figure 5a-b: P_x = 1520 nm, P_y = 1100 nm, and h = 851.327 nm, and the resulting diffraction efficiency D_{eff} = 53%. The real part of the complex refractive index for each metasurface element within the grating period is given as follows: n_1 = 3.734, n_2 = 3.74144, n_3 = 3.74318.

8. Metasurfaces with a finite number of metasurface elements

We consider an *m* x *m* array of metasurface elements and study how the quality factor of the mode supported by the finite array increases with *m* (see Figure S30). To calculate the quality factor, we calculate the scattering cross-section of the finite array and fit it to the Fano formula (see Section 1). When studying a finite metasurface array, the assumed geometrical parameters are the same as in Figure 1 of the main manuscript: $l = w$ = 963 nm and $P_x = P_y$ = 1425 nm. To reduce the simulation time, the assumed mesh in the *z*-direction is 10 nm while the mesh in the *x*- and *y*-directions is set to 20 nm. When assuming periodic boundary conditions in the x- and y-directions, the quality factor of the supported mode is 8500. Note that this quality factor value (8500) is lower as compared with the one reported in Figure 1 and 2 of the manuscript (9800). This difference in the observed quality factors is due to the fact the in the simulations shown in Figure 1, the mesh in the *z*-direction is taken to be 5 nm while the mesh in the *x*- and *y*-directions is still set to 20 nm. As seen in Figure S30, the quality factor of the supported mode monotonously increases when increasing the number of metasurface elements in the array. For a 12x12 array, the quality factor is 6000.

Next, we assume that the number of the metasurface elements is finite in the direction *parallel* to the incoming electric field while in the direction *perpendicular* to the electric field, the periodic boundary condition is assumed (see the inset of Figure S30b). The described simulation setup enables reducing the simulation time while accessing the quality factor of the metasurface for a larger number of metasurface elements n_x. As seen in Figure S30b, when the number of the metasurface elements in the direction parallel to the electric field nx is n_x = 10, the quality factor of the metasurfaces is ~7000. While when n_x = 20, the quality factor of the metasurface is slightly below 8000.

In Figure S30c, we assume that the number of the metasurface elements is finite in the direction *perpendicular* to the incoming electric field while in the direction *parallel* to the electric field, the periodic boundary condition is assumed. In this case, when n_x = 10, the quality fact of the metasurface is ~6000. Note though that in both cases where the metasurface is finite in the direction *perpendicular* or *parallel* to the electric field, for n_x = 20, the quality factor of the metasurface is ~8000.

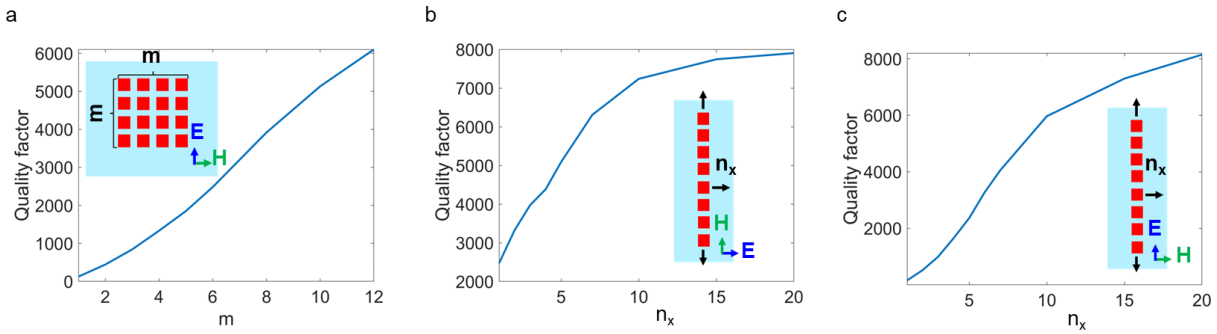


Figure S30. Quality factors of metasurfaces with a finite number of elements. a) Quality factor of an *m* x *m* metasurface array as a function of m. b) Quality factor of the metasurface, which is finite in the direction *parallel* to the incoming electric field as a function of the number of the metasurface elements in the mentioned direction n_x. In b), in the direction perpendicular to the electric field, the periodic boundary condition is assumed. c) Quality factor of the metasurface, which is finite in the direction *perpendicular* to the incoming electric field as a function of the number of the metasurface elements in the mentioned direction n_x. In c), in the direction parallel to the electric field, the periodic boundary condition is assumed.

9. Effect of potential fabrication imperfections.

Here, we investigate the effect of fabrication imperfections on the metasurface performance. To address this comment, we considered three different imperfections:

i) Tilted sidewalls
ii) Rounded corners
iii) Lossy Si.

Our simulations show that our metasurface is quite robust to possible fabrication imperfections such as tilted sidewalls or rounded corners. It may be necessary to slightly change the height of the structure depending on the exact tilt of the sidewalls. The most challenging aspect for achieving quality factors of ~10,000 would be depositing a-Si with a very low extinction coefficient ($k \sim 10^{-5}$). It is worth noting that a-Si with such an ultralow extinction coefficient has been previously demonstrated in the literature.[4] A detailed discussion of the effect of each of the listed non-idealities on the metasurface performance is discussed in what follows.

Tilted sidewalls

First, we discuss the case of the tilted sidewalls. For simplicity, we consider the case of an a-Si resonator on an SiO_2 substrate (see Figure 1 and 2 of the manuscript). We assume the period of P_x

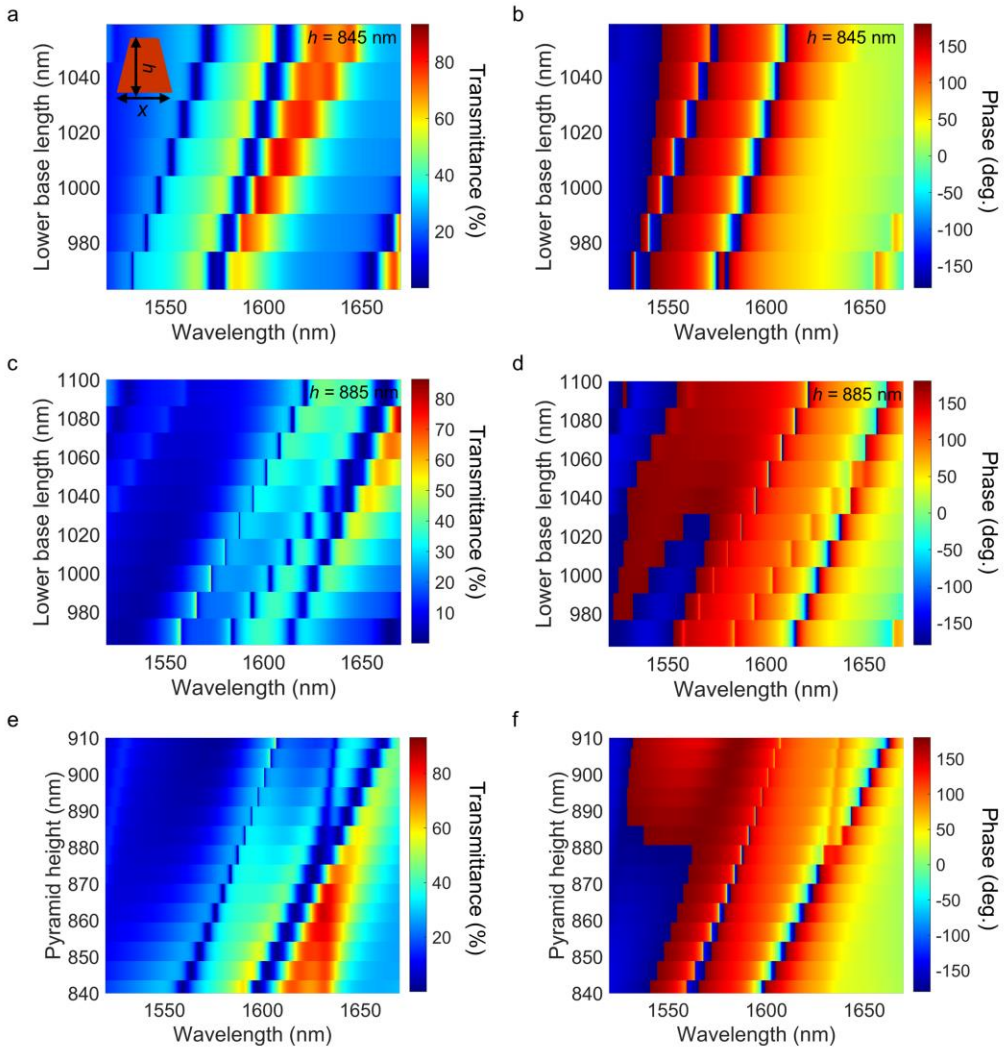


Figure S31. Influence of tilted sidewalls on the metasurface performance. In a) and b), transmittance a) and the phase of the transmitted light b) as a function of wavelength and the lower base length of the pyramid when the pyramid height is h = 845 nm. In c) and d), transmittance c) and the phase of the transmitted light d) as a function of wavelength and the lower base length of the pyramid when the pyramid height is h = 885 nm. In e) and f), transmittance e) and the phase of the transmitted light f) as a function of wavelength and the pyramid height. In e) and f), the upper base of the pyramid is 963 nm while the lower base of the pyramid is 1030 nm, which corresponds to the tilt angle of 2.27º.

= P_y = 1425 nm. Because of the tilted sidewalls, the a-Si resonator is not a rectangular parallelepiped anymore but is a truncated square pyramid (see the inset of Fig. S31a). To assess how the extent of tilt affects the supported resonances we fix the top base of the truncated a-Si pyramid as 963 nm and change the length of the bottom base. Figures S31a and S31b plot the transmittance and the phase of the transmitted light as a function of wavelength and the lower base length of the pyramid. In Figure S31a and S31b, the height of the pyramid is h = 845 nm. We

observe a significant broadening of the high-Q resonance with the length of the lower base of the pyramid. Moreover, we observe that the phase of the transmitted light exhibits a large variation in the spectral domain only for the base lengths below 1030 nm. Note that a large range of the phase variation in the spectral domain is important for exhibiting a dynamically tunable phase shift. Thus, when the pyramid height is h = 845 nm, the tilt angle should not exceed 2.27^o.

Next, we consider an a-Si truncated pyramid with a height of h = 885 nm on an SiO_2 substrate (Figure S31c and S31d). The top base of the pyramid is 963 nm. When the lower and upper bases of the pyramid are equal, we observe both high-Q and a lower-Q mode in the transmittance spectrum, but we do not observe a large phase variation in the spectral domain. We observe that the quality factor of the higher-Q resonance increases with the lower base length and achieves a peak value of ~ 4000 when the lower base length is 1030 nm (Fig. S31c). Notably, when the lower base length is increased to 1030 nm, we also observe a large phase variation in the spectral domain (Fig. S31d). Thus, when the pyramid's height is 885 nm, we observe a large variation of phase in the spectral domain even for the larger base lengths of 1100 nm that corresponds to the tilt angle of 4.43^o.

Finally, we investigate how the optical mode supported by an a-Si truncated pyramid on an SiO_2 substrate changes with the pyramid height (Figure S31e and S31f). In Figure S31e and S31f, the upper base of the pyramid is 963 nm while the lower base of the pyramid is 1030 nm.

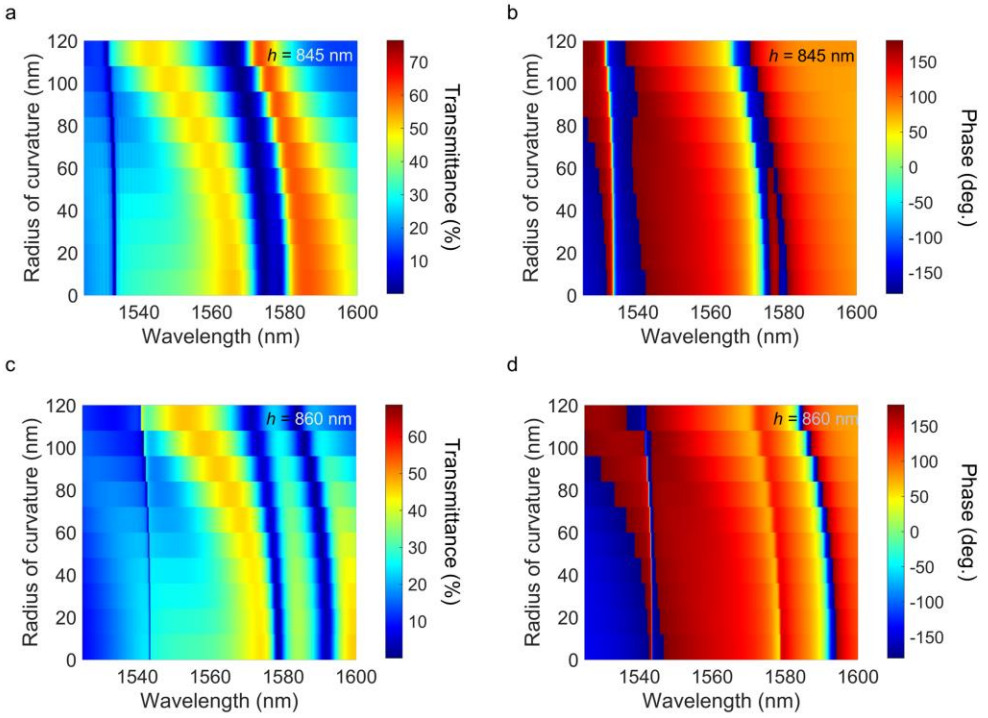


Figure S32. Influence of the rounded corners on the metasurface performance. In a) and b), transmittance a) and the phase of the transmitted light b) as a function of wavelength and the radius of curvature when the pillar height is h = 845 nm. In c) and d), transmittance c) and the phase of the transmitted light d) as a function of wavelength and the radius of the curvature when the pillar height is h = 860 nm.

We observe that both the high-Q and the lower-Q resonances red shift when increasing the pyramid height (Figure S31e and S31f). We also observe that the quality factor of the high-Q resonance increases when the pyramid height is increased from 840 nm peaking at a value of 890 nm. For the given values of the pyramid bases (963 nm and 1030 nm), a large phase variation in the spectral domain is observed for the pyramid height ranging between 850 nm and 885 nm. Thus, the designed metasurface is robust to a possible non-ideality originating from not having perfectly vertical sidewalls. Even when the sidewalls are not perfectly vertical, one may slightly increase the height of the resonator to access the mode with a high quality factor.

Rounded corners

Next, we discuss how having rounded rather than perfectly right corners affects the performance of the metasurface. Here, we consider an a-Si parallelepiped with rounded corners and bends on an SiO_2 substrate. The dimensions of the structure are the same as in Figure 1 and 2 of the manuscript. Figure S32 investigates how changing the radius of the curvature of the corners and bends affects the transmittance and phase of the transmitted light. In Figure S32a and S32b, the resonator height is h = 845 nm while in Figure S32c and S32d, the resonator height is h = 860 nm. We observe a blue shift of both high-Q and lower-Q resonances when increasing the curvature radius. The blue shift is more prominent for the lower-Q mode. As seen in Fig. R2, for the resonator height h = 845 nm, the high-Q resonance is very robust to non-ideality associated with rounded corners and bends. When the a-Si resonator height is h = 845 nm, the essential characteristics of the resonance are preserved even for a curvature radius of 120 nm (Figure S32a and S32b). When the a-Si resonator height is h = 860 nm, we observe a large variation of phase in the spectral domain for the radiuses of curvature below 100 nm (Fig. S32c). Thus, if the expected radius of curvature is above 100 nm, the resonator height needs to be below 860 nm.

Optical loss in Si

When performing experiments, non-ideal properties of materials can significantly affect the optical response of the metasurface. Here, we investigate how non-zero optical loss in a-Si affects the transmittance spectrum and phase spectrum of the transmitted. As an example, we consider a metasurface comprised of a-Si pillars on an SiO_2 substrate, which has been discussed in Figures 1 and 2 of the manuscript. We consider three different pillar heights, h = 830 nm, h = 845 nm, and h = 860 nm. For each pillar height, we plot the transmittance spectrum for three different values of the extinction coefficient of a-Si: k = 0, k = 0.0001, and k = 0.0005 (Fig. S33). We observe that the lower-Q resonances observed at longer wavelengths are practically unaffected by the introduced optical loss. On the other hand, the high-Q resonance observed at shorter wavelengths can be strongly affected by optical loss. For example, when the pillar height is h = 845 nm, for the high-Q mode, the phase of the transmitted light exhibits limited variability in the spectral domain when the extinction coefficient is k = 0.0005 (Fig. S33d). When the pillar height is h = 860 nm, introducing an extinction coefficient k = 0.0001 is sufficient for changing the spectral shape of the

transmitted phase (Fig. 3f). Our simulations also confirm (not shown here) that when the pillar height is h = 860 nm, introducing an extinction coefficient of k = 0.00001, does not affect the optical response of the metasurface. Prior research has shown that it is possible to deposit amorphous Si with such a small extinction coefficient.[4]

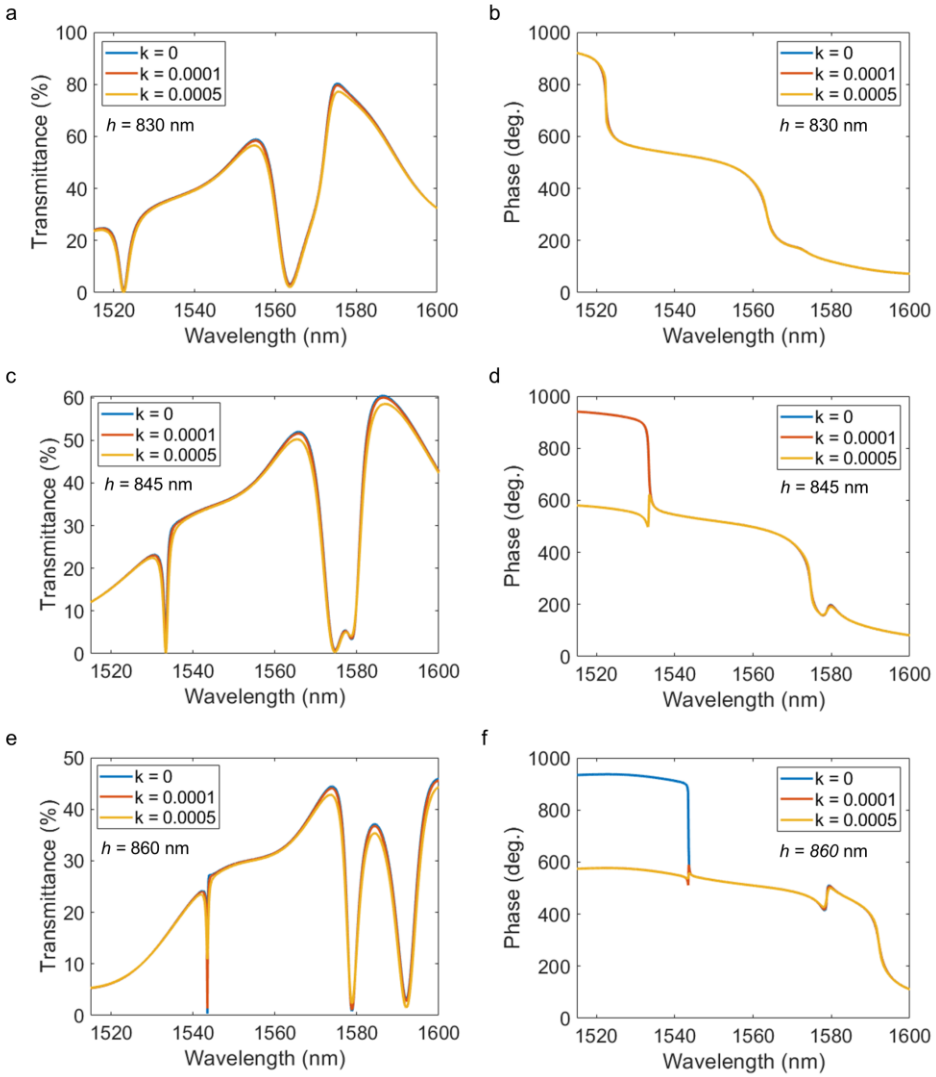


Figure S33. Influence of the material loss on the metasurface performance. In a) and b), transmittance a) and the phase of the transmitted light b) as a function of wavelength for different values of the extinction coefficient k when the pillar height is h = 830 nm. In c) and d), transmittance c) and the phase of the transmitted light d) as a function of wavelength for different values of the extinction coefficient k when the pillar height is h = 845 nm. In e) and f), transmittance e) and the phase of the transmitted light f) as a function of wavelength for different values of the extinction coefficient k when the pillar height is h = 860 nm.

10. High-efficiency reflective high-Q metasurfaces.

By adding a Au back reflector to the designed transmissive metasurface we can attain high-efficiency high-Q reflective metasurfaces. The unit cell of the proposed metasurface design is shown in Figure S34a. The metasurface unit cell consists of an Au back reflector, followed by an SiO_2 spacer on top of which we place an a-Si pillar. By appropriately choosing the thickness of the SiO_2 spacer we obtain high-efficiency high-Q reflective metasurfaces.

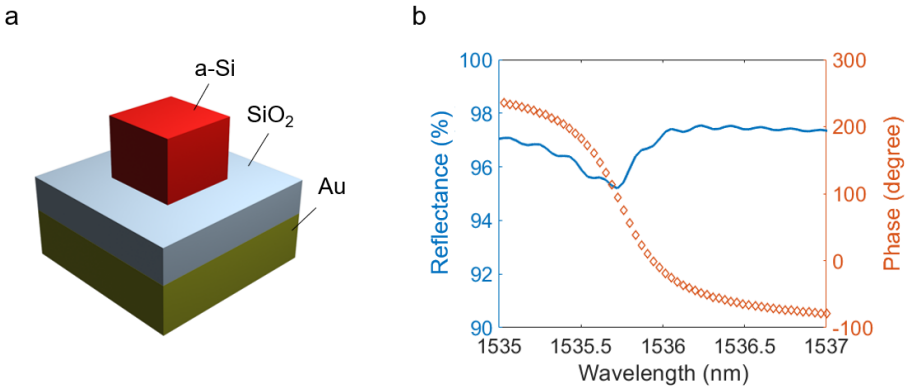


Figure S34. High-efficiency transmissive metasurfaces. a) Schematic of the unit cell of the high efficiency transmissive metasurface. In a), the length and width of the a-Si pillar are taken to be $l = w = 963$ nm. The metasurface period is $P_x = P_y = 1425$ nm. the thickness of the SiO_2 spacer is 516 nm while Au is optically thick. b) Phase and reflectance spectra for the designed metasurface.

References

[1] L. Novotny, B. Hecht, *Principles of nano-optics*, Cambridge University Press, Cambridge **2012**.

[2] E. Melik-Gaykazyan, K. Koshelev, J.-H. Choi, S. S. Kruk, A. Bogdanov, H.-G. Park, Y. Kivshar, *Nano Letters* **2021**, 21, 1765.

[3] P. Thureja, G. K. Shirmanesh, K. T. Fountaine, R. Sokhoyan, M. Grajower, H. A. Atwater, *ACS Nano* **2020**, 14, 15042.

[4] R. Birney, J. Steinlechner, Z. Tornasi, S. MacFoy, D. Vine, A. S. Bell, D. Gibson, J. Hough, S. Rowan, P. Sortais, S. Sproules, S. Tait, I. W. Martin, S. Reid, *Physical Review Letters* **2018**, 121, 191101.